Received: 30 May 2022 | Revised: 16 September 2022 | Accepted: 7 November 2022
DOI: 10.1002/nme.7170

RESEARCH ARTICLE

WILEY

Finite element modeling of plastic hinges based on ductility demand-capacity method using nonlinear material for dynamic analysis

Karol Grębowski[1] | **Krzysztof Wilde**[2] | **Mikołaj Miśkiewicz**[2]

[1]Department of Technical Fundamentals of Architectural Design, Faculty of Architecture, Gdańsk University of Technology, Gdańsk, Poland

[2]Department of Mechanics of Materials and Structures, Faculty of Civil and Environmental Engineering, Gdańsk University of Technology, Gdańsk, Poland

Correspondence
Karol Grębowski, Department of Technical Fundamentals of Architectural Design, Faculty of Architecture, Gdańsk University of Technology, Narutowicza 11/12, 80-233 Gdańsk, Poland.
Email: karol.grebowski@pg.edu.pl

Abstract

The article discusses modeling plastic hinges in reinforced concrete intermediate supports using finite elements methods. The ductility demand-capacity method was used to determine the geometrical parameters of cross-section plasticization zones, their ability to move and rotate, as well as their ductility. Due to the varied geometry and stiffness of the supports and their nonlinear behavior under dynamic load, this method was concluded to be imperfect. Therefore, an improved algorithm was proposed by determining the main parameters of plastic hinges depending on the degree of concrete degradation according to Lubliner's assumptions. The new algorithm has been implemented in the form of mathematical equations. It was subsequently used, at the structure design stage, to perform numerical calculations based on the finite element method.

KEYWORDS

concrete damaged-plasticity model, ductility demand-capacity method, explicit dynamics, finite element modeling, plastic hinges, reinforcement concrete support

1 | INDRODUCTION

Designing concrete and reinforced concrete elements is based on standard regulations, which are primarily based on the results of experimental research. The proposed formulas usually result from linear analysis with numerous safety factors included. Such a description of the behavior of concrete and reinforced concrete elements is oversimplified, especially if these elements are thoroughly analyzed. Therefore, it is necessary to account for nonlinear behavior during the loading process, as well as material heterogeneity.

As the experimental studies of Kostovos and Newman[1] and Kupfer et al.[2] show, concrete behavior depends on whether we analyze simple or complex stress conditions. With uniaxial compression, the concrete exhibits linear and elastic behavior up to about 30% of its compressive strength f_c. When this value is exceeded, its behavior becomes nonlinear. This nonlinear stress increment, before reaching f_c, is called *hardening*. When the compression strength value is reached, the curve drops until the sample is destroyed—the material degrades and the stiffness levels start falling (*softening*). In the $0.3f$ to $0.75f_c$ range, microcracks develop as a result of connections breaking between individual components, additionally, the cracks around the aggregated grains start to merge. The development of microcracks stabilizes once stress reaches $0.75f_c$. At this point, damage starts to develop rapidly. The cracks in the grout join with the cracks formed at the

---

interface between the aggregate and the grout, resulting in the formation of cracks parallel to the direction of applied load. Sometimes, instead of running parallel to the load, the cracks can take the form of zigzags, which depend on the height of the sample. Further development of the cracks leads to the destruction of the sample. For low-strength concretes, the decrease in stiffness after reaching f_c is relatively small.

However, as strength increases, the stiffness decreases rapidly and the material becomes increasingly brittle. The curve shape is also influenced by the load application speed. An increase in the load application speed leads to an increase in concrete strength.

In the case of uniaxial tensioning, the concrete behaves similarly, the difference being that development of microcracks has a much greater impact on its properties. Concrete exhibits linear and elastic behavior in the range of about 60% of its tensile strength f_t. It is assumed that this is the value at which microcracks start propagating (in the direction perpendicular to the applied force), which in consequence leads to a sudden drop in load-bearing capacity and destruction of the sample. The development of microcracks results in the appearance of discontinuity of displacements and failure zones are made visible by location. The low concrete tensile strength is mainly due to the low strength of the grout-aggregate joint, which is much lower than the strength of the grout itself. The cracks are usually created and developed there, which leads to the destruction of the material. In contrast to compression, cracks develop in the direction perpendicular to the direction of the maximum applied tensile stress.

The behavior of the concrete can only be regarded as linear within a small strain range. Concrete is a brittle or quasi-brittle material. It is characterized by a significant and sudden drop in stress once the maximum load-bearing capacity is reached in both compression and tension. This is additionally accompanied by a concentration of stains in small areas; the so-called stain location zones. Cyclical load applications also lead to a significant reduction in stiffness. Subsequent load and strain cycles show a decrease in material stiffness (reduction of the curve angle) for successive loops. This decrease in stiffness results from the formation and propagation of cracks in concrete. This phenomenon is called stiffness degradation or elastic degradation. Cyclical load application is accompanied by a strong nonlinear stress–strain curve. Clear hysteresis loops are also observed, which are a sign of internal friction and dissipation of internal energy. As a result of the change in the load direction, from tension to compression, the cracks perpendicular to the load direction are closed. As a result, the material "regains" its initial stiffness. This phenomenon is called *stiffness recovery*. Test results for periodically loaded concrete elements are available in the literature. Among others, Hordijk[3] and Perdikaris and Romeo[4] discussed these issues. They tested concrete beams subjected to cyclic bending.

Computational models for the non-elastic analysis of such material should correctly simulate a decrease in load-bearing capacity in the weakening phase, a reduction in stiffness during cyclic loading, and the formation and development of plastic strains. The numerical results should also be independent of the FEM grid used. Unfortunately, the application of classical constitutive laws with weakening, combined with the finite element method, leads to incorrect results. The force-displacement curves obtained depend on the adopted FEM grid and the deformations concentrate in one-element-wide bands. To prevent this, it is necessary to expand classical constitutive models by introducing combined models which take into account the so-called damage parameter.

In the simplest case, the set of damage parameters can be a scalar value, see Mazars.[5] Vectors can also be used (see Krajcinovic and Fonseka[6]) together with second-order tensors (see Dragon and Mróz[7] and Carol et al.[8,9]) or fourth-order tensors (see Simo and Ju[10] and Carol et al.[11]). Only the application of second and higher-order tensors allows one to properly simulate the material anisotropy. Accounting for the opening and closing of cracks during the stretching and compression processes constitutes a significant problem in modeling concrete. In such a case, the problem of different material stiffnesses, in compression and stretching, emerges. The most common way to solve this problem is to use projection operators (usually fourth-order tensors) to divide the strain (or tension) tensor into positive and negative parts, see Ortiz[12] and Simo and Ju.[10]

The idea behind "combined" models is to include the characteristics of elastic–plastic models and elastic degradation models in a single formula. Elastic–plastic laws can account for permanent deformations. The laws construed within the framework of damage mechanics, in their turn, assume that the deformations in the process of loading and unloading are fully reversible, but they can simulate isotropic or anisotropic degradation of material stiffnesses. There are several ways to combine both theories. The simplest method, and the most common one, is to define the plasticity condition in the effective stain space. In this method, degradation depends on the strain tensor and has no direct impact on ductility. Despite their simplicity, models built in this way (see Pamin and de Borst[13] and Lee and Fenves[14]) are very efficient. The second method consists of defining degradation in a form analogous to the elastic–plastic law. Thus, we usually end up with models containing two plasticity surfaces. For compression usually was a classic elastic–plastic function, while for tension a load function with degradation parameters was introduced, see Luccioni et al.[15] and Hansen et al.[16,17] The last way of combining the two formulations consists of making the degradation overtly dependent on the growth of the plastic deformation tensor, see Ortiz[12] and Meschke et al.[18]

Works on elastic–plastic models with elastic degradation began in the 1970s and 1980s. First such models were presented by Bažant and Kim,[19] Dragon and Mróz,[7] and by Ortiz,[12] Klisiński and Mróz[20] proposed a model in which they applied the division of deformations into elastic, plastic, and degradation-related components. Degradation was linked to ductility by defining the surface for both criteria and the appropriate interaction laws between them. Lubliner et al.[21] presented an improved formulation based on the Drucker–Prager criterion. The flow law was adopted in the form of the Coulomb–Mohr criterion. In this model, two degradation parameters and a plastic degradation parameter linked to the rigidity tenor were applied. For reinforced concrete elements, these parameters help to model the contact between steel and concrete, which influences the behavior of the whole element, similar to Chróścielewski et al.[22] Taking into account the impact from a dynamic load, numerical calculations are possible thanks to the application of plastic-degradation concrete modeling according to Lubliner's assumptions (e.g., in the form of an earthquake).

For years, designing bridge supports resistant to earthquake loads using the finite element method has been one of the most demanding challenges for designers and researchers. The basic calculation method is elastic and plastic analysis, see Grassl and Jirásek.[23] The elastic theory method should be applied if and only if it is proved beyond doubt that the material (reinforcement in the case of reinforced concrete supports) is not capable of reaching sufficient plasticity and the cross-section of the support element in critical sections has sufficient freedom of rotation to form a plastic hinge. If these conditions are not met, plastic analysis is necessary for seismic design, see Grębowski et al.[24,25] Plastic analysis methods lead to optimal design by using plastic reserves in the form of plastic hinges.

A plastic hinge does not allow for rotation under loads smaller than that which plasticizes the hinge, but under greater loads it transmits the boundary moment and allows for rotation, see Zhao et al.[26] For supports made of concrete, taking into account the concept of plastic hinges, correct plastic analysis requires the use of a plastic-degradable model of concrete. In this model, during element loading, the load-bearing capacity limit is reached as a result of degradation of the material from the increase in external load, and consequently, the load-bearing capacity is lost due to the increase in plastic deformation, see Lubliner et al.,[21] Lasowicz et al.,[27] Stręk et al.,[28] and Oller et al.[29] This is a very important element of the analysis, thanks to the location of the place where the support material degrades the fastest and to the greatest extent, it is possible to determine the place where plastic hinges are formed. This is due to the fact that where concrete loses its load-bearing capacity, reinforcement (i.e., steel) starts to play a major role in transferring the loads.

The ABAQUS and LS-DYNA programs were used to perform effective numerical analysis. First, the concrete damage plasticity (CDP) model was validated in the ABAQUS software. On this basis, the CDP model parameters were calibrated based on laboratory tests and numerical analyses in the form of axial compression of the specimen and a three-point flexural test. The calibration of parameters determining the properties of concrete, described by the CDP model, included compressive degradation d_c, tensile degradation d_t, dilatation angle ψ, eccentricity e, biaxial/uniaxial compression plastic strain ratio f_{b0}/f_{c0}, parameter K, and viscosity parameter μ. The elaborated CDP model was then updated by considering the reinforcement bars. In the second stage, the obtained parameters were verified using the LS-DYNA software by comparing the parameters of the CDP model with reinforcement obtained in the ABAQUS software. The verification was carried out for the highest support of the V17 viaduct—support no. 8, 70 m high. After a positive verification, a complete (detailed) model of the V17 viaduct was prepared in the LS-DYNA software. This modeling procedure sequence was adopted because the LS-DYNA software was found to be a more effective and efficient tool for researching fast-changing phenomena with the nature of generated waves propagation, for example, an earthquake load. Therefore, the final and ultimate numerical simulations of the dynamic response of the full V17 viaduct model to the earthquake impact were carried out entirely in the LS-DYNA software.

This article presents the modeling of plastic hinges in reinforced concrete bridge supports using finite elements based on the plastic-degradation model of reinforced concrete. Based on the ductility demand-capacity (DDC) method, geometrical parameters of plastification zones in support cross-sections, their displacement and rotation capacity, as well as their ductility were determined. Due to the differences in support geometry and stiffness and their nonlinear behavior under dynamic load, this method was found to be far from perfect. Therefore, we proposed a new algorithm for determining the main parameters of plastic hinges, depending on the degree of concrete degradation, according to Lubliner's assumptions. The new algorithm has been implemented in the form of mathematical equations. Further in this work, we used it for numerical tests based on the finite element method. The new algorithm was used to design the actual structure of viaducts of the Istanbul Northern Marmara Highway ring road implemented by the authors.

2 | THE PROJECT

In 2014–2018, as a result of the expansion of the city of Istanbul in Turkey, a project consisting of building a northern ring road, called Northern Marmara Highway, was implemented. Istanbul is the only city in the world spanning two continents: Europe and Asia. Both continents are separated by the Bosporus. To the north is the Black Sea and to the south is the Marmara Sea, from which the ring road takes its name.

Istanbul is located in a high earthquake risk area. In 1999, an earthquake of 7.6 on the Richter scale occurred in the province of Kocaeli, a few dozen kilometers from Istanbul. Therefore, the impact of the dynamic load from an earthquake had to be taken into account at the design stage. All the more so as studies from 2000 showed that there is a 70% risk of a 7-degree Richter earthquake occurring in Istanbul by 2030, thus the resistance of the viaduct structure is likely to be tested in the future.

The main objective of the study was to develop innovative solutions for the construction of intermediate supports for the Istanbul ring road viaducts in terms of determining rigidity in relation to seismic requirements for three levels of earthquake intensities according to Turkish DLH 2008 normative documents. The Northern Marmara Highway ring road consists of 36 elements (from V1 to V36). The V17 viaduct was selected for research since it exhibits the most variation in support height. The studied facility is located on the western side of the ring road. The total length of the viaduct is 640 m. The bridge is divided into 13 parts. The span of the first and last bay is 45 m, while the span of the middle bay is 50 m. The platform is based on 14 supports. The highest support is 70 m.

The concept shape of the original support assumed that each support was made as a solid element, with an I-section over the whole height. The first research stage consisted of checking the distribution of internal forces on individual supports. For objects with a significantly variable height of intermediate supports, redistribution of the internal forces generated during earthquakes was the main issue. The use of supports with identical stiffness along the whole height results in very big forces in the lowest supports and as a result tears them out (Figure 1).

As a result of this problem, an innovative concept for shaping the intermediate support structure with variable geometry and stiffness was proposed at the design stage, which assumes that the support would consists of two parts—rigid (lower) and flaccid (upper) parts. The upper part of the support consists of two flaccid reinforced concrete columns with a fixed height of 21 m. The lower part of the support consists of a rigid I-section. At the top of the support, there is a girt beam on which the platform is based and which is equipped with a reinforced concrete buffer to absorb the impact of the platform against the support. The transition zone uses a reinforced concrete shelf to connect the rigid and flaccid parts of the support (Figure 2).

The new support concept, with variable geometry and stiffness, must meet the design requirements provided in the Turkish normative documents for the three calculated earthquake intensity levels (D1, D2, D3). For level D1, the flyover should not be damaged in any way. For level D2, the viaduct may be damaged, but the damage should be minor so that

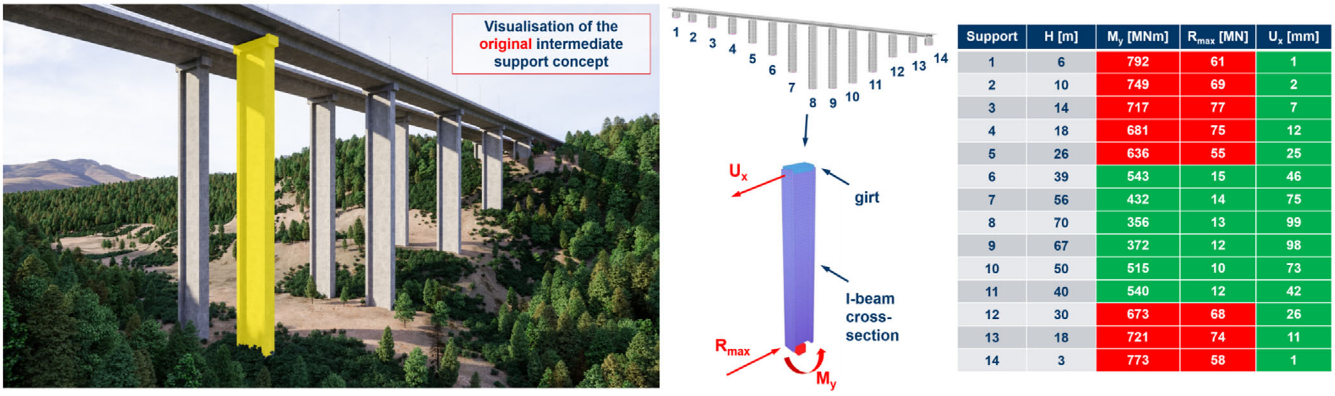

Support	H [m]	M_y [MNm]	R_{max} [MN]	U_x [mm]
1	6	792	61	1
2	10	749	69	2
3	14	717	77	7
4	18	681	75	12
5	26	636	55	25
6	39	543	15	46
7	56	432	14	75
8	70	356	13	99
9	67	372	12	98
10	50	515	10	73
11	40	540	12	42
12	30	673	68	26
13	18	721	74	11
14	3	773	58	1

FIGURE 1 Original support concept

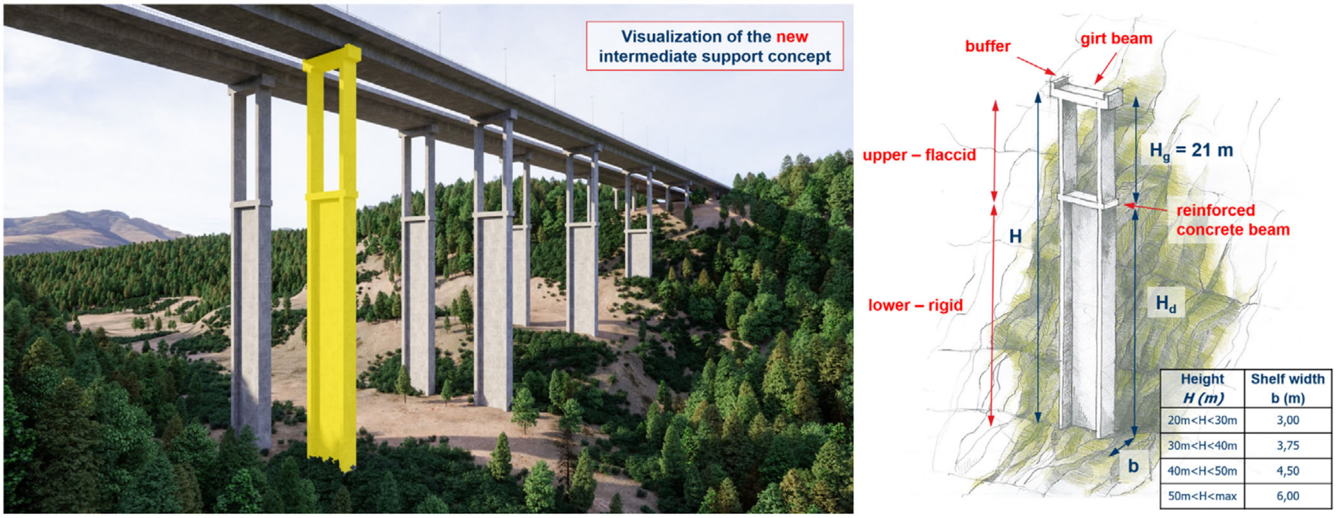

Height *H (m)*	Shelf width b (m)
20m<H<30m	3,00
30m<H<40m	3,75
40m<H<50m	4,50
50m<H<max	6,00

FIGURE 2 New support concept

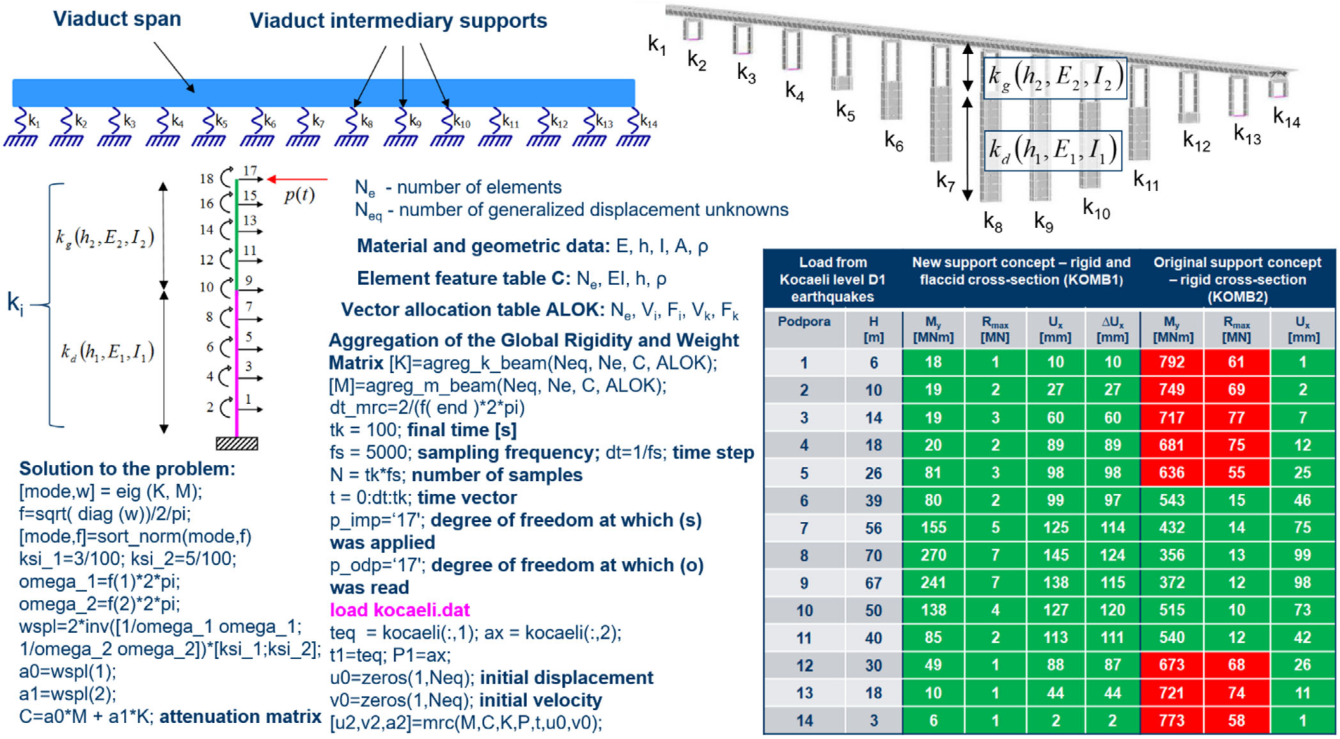

N_e - number of elements
N_{eq} - number of generalized displacement unknowns

Material and geometric data: E, h, I, A, ρ

Element feature table C: N_e, EI, h, ρ

Vector allocation table ALOK: N_e, V_i, F_i, V_k, F_k

```
Solution to the problem:
[mode,w] = eig (K, M);
f=sqrt( diag (w))/2/pi;
[mode,f]=sort_norm(mode,f)
ksi_1=3/100; ksi_2=5/100;
omega_1=f(1)*2*pi;
omega_2=f(2)*2*pi;
wspl=2*inv([1/omega_1 omega_1;
1/omega_2 omega_2])*[ksi_1;ksi_2];
a0=wspl(1);
a1=wspl(2);
C=a0*M + a1*K; attenuation matrix
```

```
Aggregation of the Global Rigidity and Weight
Matrix [K]=agreg_k_beam(Neq, Ne, C, ALOK);
[M]=agreg_m_beam(Neq, Ne, C, ALOK);
dt_mrc=2/(f( end )*2*pi)
tk = 100; final time [s]
fs = 5000; sampling frequency; dt=1/fs; time step
N = tk*fs; number of samples
t = 0:dt:tk; time vector
p_imp='17'; degree of freedom at which (s)
was applied
p_odp='17'; degree of freedom at which (o)
was read
load kocaeli.dat
teq  = kocaeli(:,1); ax = kocaeli(:,2);
t1=teq; P1=ax;
u0=zeros(1,Neq); initial displacement
v0=zeros(1,Neq); initial velocity
[u2,v2,a2]=mrc(M,C,K,P,t,u0,v0);
```

Load from Kocaeli level D1 earthquakes		New support concept – rigid and flaccid cross-section (KOMB1)				Original support concept – rigid cross-section (KOMB2)		
Podpora	H [m]	M_y [MNm]	R_{max} [MN]	U_x [mm]	ΔU_x [mm]	M_y [MNm]	R_{max} [MN]	U_x [mm]
1	6	18	1	10	10	792	61	1
2	10	19	2	27	27	749	69	2
3	14	19	3	60	60	717	77	7
4	18	20	2	89	89	681	75	12
5	26	81	3	98	98	636	55	25
6	39	80	2	99	97	543	15	46
7	56	155	5	125	114	432	14	75
8	70	270	7	145	124	356	13	99
9	67	241	7	138	115	372	12	98
10	50	138	4	127	120	515	10	73
11	40	85	2	113	111	540	12	42
12	30	49	1	88	87	673	68	26
13	18	10	1	44	44	721	74	11
14	3	6	1	2	2	773	58	1

FIGURE 3 Our proprietary program describing a discrete model of intermediate support with variable geometry and stiffness

it can be repaired within a few months with minor traffic restrictions. For level D3, however, controlled damage to the intermediate supports should take place at the top of the supports through the formation of plastic hinges. The platform must not fall from the hinges.

To carry out efficient parametric tests showing the distribution of internal forces depending on particular levels of earthquake intensity, we created an original program using differential equations to describe a linear model of intermediate supports with variable geometry and rigidity, together with a platform in the form using Matlab software (Figure 3).

Based on the results obtained, it was proven that the newly adopted indirect support concept improves the redistribution of internal forces on individual supports of the facility under seismic load from levels D1 and D2. For the viaduct's end supports, the bending moments have decreased, on average from 721 to 20 MN m, and the bearing reaction decreased, on average from 42 to 2 MN.

The distribution forces on individual supports were corrected at the expense of increasing the displacement of the upper part of the supports at the point of connection between the girt and the bridge. The deflection of intermediate supports under load from D1 and D2 levels are too small to make the support plastic. For these two load levels, the design conditions are met. However, for the extreme shocks experienced at level D3 it is the upper support part that should ensure the safety of the structure despite the large deflections, by designing the places where the plastic hinges are formed.

Our analysis, performed using our proprietary programme, allowed us to check in detail the design requirements for level D3, which assumes that the controlled damage should take place in the upper part of the intermediate supports through the formation of plastic hinges. To perform such an analysis it is necessary to take into account the plastic-degradation model of concrete with reinforcement.

3 CONCRETE DAMAGED-PLASTICITY MODEL FORMULATION

The damaged-plastic model of the material was first proposed, under the name of the Barcelona model, by Lubliner et al.[21] Lubliner proved that an increasing external load leads to the degradation of the material, and hence the loss of its load bearing capacity results from increasing plastic deformations.

The cou pling of the elastic–plastic characteristics of the material and descriptions of damage to the material is achieved by means of the constitutive equations of the theory of plasticity by the effective stresses. From the perspective of the incremental theory of plasticity, the damaged-plastic model is characterized by:

- A yield surface that is an extension of the classical Drucker–Prager model, in which the meridians (forming a yield surface in a meridian cross-section) are lines, while the deviatoric cross section is non-circular.
- A non-associative flow rule, in which plastic deformations are determined on the basis of yield surface plastic potential different from the yield surface.
- Nonlinear isotropic hardening rules of a bimechanical type (independent of compression and tension), based on the hypothesis of deformation hardening.

The main purpose of the model is to define the mechanism of concrete failure in uniaxial states and then to correctly transform this mechanism to represent more complex, multi-axial states. One of the basic assumptions of the damaged-plastic model is the strain rate decomposition:

$$\dot{\varepsilon} = \dot{\varepsilon}^{\mathrm{el}} + \dot{\varepsilon}^{\mathrm{pl}}, \tag{1}$$

where $\dot{\varepsilon}$ is the strain-rate of total deformation, $\dot{\varepsilon}^{\mathrm{el}}$ is the strain-rate of elastic strains, and $\dot{\varepsilon}^{\mathrm{pl}}$ is the strain-rate of plastic deformation. Constitutive relationships are described by the following formula:

$$\boldsymbol{\sigma} = (1-d)\boldsymbol{D}_0^{\mathrm{el}} : \left(\varepsilon - \varepsilon^{\mathrm{pl}}\right) = \boldsymbol{D}^{\mathrm{el}} : \left(\varepsilon - \varepsilon^{\mathrm{pl}}\right), \tag{2}$$

where $\boldsymbol{D}_0^{\mathrm{el}}$ is the initial stiffness of the undamaged material. Stiffness degradation is described by the formula:

$$\boldsymbol{D}^{\mathrm{el}} = (1-d)\boldsymbol{D}_0^{\mathrm{el}}, \tag{3}$$

where d is a scalar stiffness degradation variable that ranges from 0 to 1. A value of 0 indicates that the material is undamaged, while a value of 1 indicates that the material is completely damaged. This parameter makes it possible to combine the failure mechanism of cracking and crushing with the reduction of material stiffness. It differs in the state of compression and tension. Taking into account effective stresses, the following formula is obtained:

$$\overline{\boldsymbol{\sigma}} = \boldsymbol{D}_0^{\mathrm{el}} : \left(\varepsilon - \varepsilon^{\mathrm{pl}}\right). \tag{4}$$

According to the above formula, Cauchy stresses are related to the effective stresses by the degradation variable:

$$\boldsymbol{\sigma} = (1-d)\overline{\boldsymbol{\sigma}}, \tag{5}$$

where $(1-d)$ is the relation of the effective area carrying the load, that is, the total area minus the damaged area to the total cross-sectional area. The increase in the surface of plastic degradation is described by two variables of strengthening $\tilde{\varepsilon}_t^{\text{pl}}$ and $\tilde{\varepsilon}_c^{\text{pl}}$, where the index *t* (tension) denotes parameters related to stretching, and the index *c* (compression) denotes parameters related to compression. These variables are used in determining the equivalent plastic strains:

$$\tilde{\varepsilon}^{pl} = \begin{bmatrix} \tilde{\varepsilon}_t^{\text{pl}} \\ \tilde{\varepsilon}_c^{\text{pl}} \end{bmatrix}. \tag{6}$$

The formula describing the plastic degradation function that represents the failure area in the effective stress space is expressed as:

$$F\left(\overline{\boldsymbol{\sigma}}, \tilde{\varepsilon}^{\text{pl}}\right) \leq 0. \tag{7}$$

According to the principle of non-associated plastic flow, the plastic flow of the material causes a plastic potential in the effective stress space:

$$\dot{\varepsilon}^{\text{pl}} = \dot{\lambda}\frac{\partial G(\overline{\boldsymbol{\sigma}})}{\partial \overline{\boldsymbol{\sigma}}}, \tag{8}$$

where $\dot{\lambda}$ is a non-negative plastic multiplier. The parameter $\dot{\lambda}$ and the function F fulfill the Kuhn-Tucker conditions according to the dependencies:

$$\dot{\lambda}F = 0, \quad \dot{\lambda} \geq 0, \quad F \leq 0. \tag{9}$$

On the basis of all formulas discussed in this section, it can be concluded that the elastic–plastic work of the material in the model is described with the use of effective stresses, as well as reinforcement variables.

3.1 | Material degradation function

In the damaged-plastic model, material degradation means the degradation of stiffness. It is first determined for the uniaxial work of the material and then converted for a multi-axial work. In the uniaxial state, the stresses can be written as functions:

$$\begin{aligned} \sigma_t &= \sigma_t\left(\tilde{\varepsilon}_t^{\text{pl}}, \dot{\tilde{\varepsilon}}_t^{\text{pl}}, \theta, f_i\right), \\ \sigma_c &= \sigma_c\left(\tilde{\varepsilon}_c^{\text{pl}}, \dot{\tilde{\varepsilon}}_c^{\text{pl}}, \theta, f_i\right), \end{aligned} \tag{10}$$

where $\dot{\tilde{\varepsilon}}_t^{\text{pl}}, \dot{\tilde{\varepsilon}}_c^{\text{pl}}$ are the velocities of equivalent plastic deformations, while $\tilde{\varepsilon}_t^{\text{pl}}, \tilde{\varepsilon}_c^{\text{pl}}$ are the equivalent plastic deformations:

$$\begin{aligned} \tilde{\varepsilon}_t^{\text{pl}} &= \int_0^t \dot{\tilde{\varepsilon}}_t^{\text{pl}}\, dt, \\ \tilde{\varepsilon}_c^{\text{pl}} &= \int_0^t \dot{\tilde{\varepsilon}}_c^{\text{pl}}\, dt. \end{aligned} \tag{11}$$

The parameter θ is the temperature, and the parameter $f_i(i = 1, 2, 3, \dots)$ represents additional variables. The velocities of plastic deformation for the uniaxial state can be expressed by the following formulas:

$$\begin{aligned} \dot{\tilde{\varepsilon}}_t^{\text{pl}} &= \dot{\varepsilon}_{11}^{\text{pl}}, \\ \dot{\tilde{\varepsilon}}_c^{\text{pl}} &= -\dot{\varepsilon}_{11}^{\text{pl}}, \end{aligned} \tag{12}$$

where the index *t* represents the uniaxial tension state, while the index *c* denotes the uniaxial compression state.

Figure 4 shows the stress–strain relationship—concrete in uniaxial tension and compression.

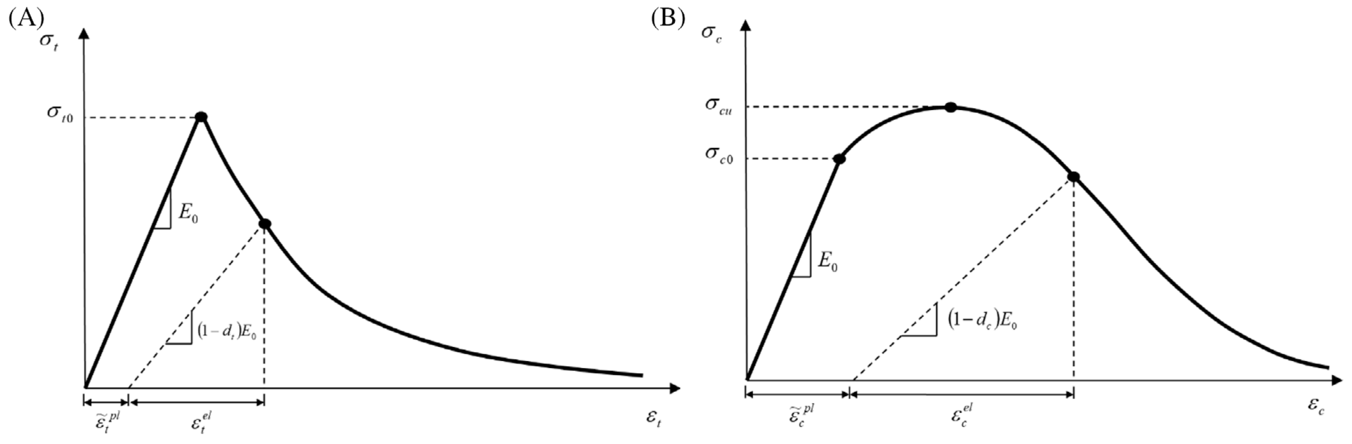

FIGURE 4 Concrete in uniaxial (A) tension and (B) compression

Degradation for compression and tension is different. The only similarity is that the result of degradation increases with the build-up of plastic deformation. Independent variables were introduced that describe the response of the material undergoing degradation in order to test the response of the material. These are uniaxial damage variables d_t and d_c, which are a function of plastic deformation, temperature, and additional variables according to the formula:

$$\begin{aligned} d_t &= d_t\left(\tilde{\varepsilon}_t^{\mathrm{pl}}, \theta, f_i\right), \quad 0 \le d_t \le 1, \\ d_c &= d_c\left(\tilde{\varepsilon}_c^{\mathrm{pl}}, \theta, f_i\right), \quad 0 \le d_c \le 1. \end{aligned} \tag{13}$$

The stress–strain relationships in the case of a uniaxial state are represented by the following formula:

$$\begin{aligned} \sigma_t &= (1-d_t)\,E_0\left(\varepsilon_t - \tilde{\varepsilon}_t^{\mathrm{pl}}\right), \\ \sigma_c &= (1-d_c)\,E_0\left(\varepsilon_c - \tilde{\varepsilon}_c^{\mathrm{pl}}\right). \end{aligned} \tag{14}$$

On the basis of the above graphs, the size of the failure surface is illustrated by the uniaxial effective cohesion stresses:

$$\begin{aligned} \overline{\sigma}_t &= \frac{\sigma_t}{(1-d_t)} = E_0\left(\varepsilon_t - \tilde{\varepsilon}_t^{\mathrm{pl}}\right), \\ \overline{\sigma}_c &= \frac{\sigma_c}{(1-d_c)} = E_0\left(\varepsilon_c - \tilde{\varepsilon}_c^{\mathrm{pl}}\right). \end{aligned} \tag{15}$$

3.2 | Plasticity condition

The plasticity condition in the plastic-degradation model is expressed using effective stresses:

$$F\left(\overline{\boldsymbol{\sigma}}, \tilde{\varepsilon}^{\mathrm{pl}}\right) = \frac{1}{1-\alpha}\left(\overline{q} - 3\alpha\overline{p} + \beta\left(\tilde{\varepsilon}^{\mathrm{pl}}\right)\left\langle \hat{\overline{\sigma}}_{\max}\right\rangle - \gamma\left\langle -\hat{\overline{\sigma}}_{\max}\right\rangle\right) - \overline{\sigma}_c\left(\tilde{\varepsilon}_c^{\mathrm{pl}}\right) \le 0, \tag{16}$$

where α and β denote dimensionless material constants, and $\overline{p}$ is the effective hydrostatic pressure:

$$\overline{p} = -\frac{1}{3}\overline{\boldsymbol{\sigma}} : I, \tag{17}$$

where $\overline{\boldsymbol{\sigma}}$ is the equivalent effective Mises stress.

$$\overline{q} = \sqrt{\frac{3}{2}\overline{\boldsymbol{S}} : \overline{\boldsymbol{S}}}, \tag{18}$$

where $\overline{\boldsymbol{S}}$ is the deviatorial part of the effective stress tensor $\overline{\boldsymbol{\sigma}}$:

$$\overline{S} = \overline{p}\boldsymbol{I} + \overline{\boldsymbol{\sigma}}. \tag{19}$$

$\hat{\overline{\sigma}}_{\max}$ denotes the algebraic maximum of the eigenvalue $\overline{\sigma}$, $\boldsymbol{I}$ is a diagonal unit matrix. The function $\beta\left(\tilde{\varepsilon}^{\mathrm{pl}}\right)$ is expressed by the equation:

$$\beta\left(\tilde{\varepsilon}^{\mathrm{pl}}\right) = \frac{\overline{\sigma}_c\left(\tilde{\varepsilon}_c^{\mathrm{pl}}\right)}{\overline{\sigma}_t\left(\tilde{\varepsilon}_t^{\mathrm{pl}}\right)}(1-\alpha) - (1+\alpha), \tag{20}$$

where $\overline{\sigma}_c$ and $\overline{\sigma}_t$ are the effective cohesive stresses in the states of tension and compression. The constant α is expressed by the formula:

$$\alpha = \frac{\sigma_{b0} - \sigma_{c0}}{2\sigma_{b0} - \sigma_{c0}}. \tag{21}$$

The parameter γ is used in a plastic state only in triaxial compression when $\hat{\overline{\sigma}}_{\max} < 0$. It is determined by comparing the yield condition for the meridians of tension and compression. The tension meridian (TM) is a place in the stress space that must fulfill the condition:

$$\hat{\overline{\sigma}}_{\max} = \hat{\overline{\sigma}}_1 > \hat{\overline{\sigma}}_2 = \hat{\overline{\sigma}}_3. \tag{22}$$

The compression meridian (CM), on the other hand, is a place in the stress space that must fulfill the condition:

$$\hat{\overline{\sigma}}_{\max} = \hat{\overline{\sigma}}_1 = \hat{\overline{\sigma}}_2 > \hat{\overline{\sigma}}_3, \tag{23}$$

where $\hat{\overline{\sigma}}_1, \hat{\overline{\sigma}}_2, \hat{\overline{\sigma}}_3$ denote the eigenvalues of the effective stress tensor. Along the meridians of tension and compression, the following dependencies must be fulfilled:

$$\begin{aligned} \left(\hat{\overline{\sigma}}_{\max}\right)_{\mathrm{TM}} &= \frac{2}{3}\overline{q} - \overline{p}, \\ \left(\hat{\overline{\sigma}}_{\max}\right)_{\mathrm{CM}} &= \frac{1}{3}\overline{q} - \overline{p}. \end{aligned} \tag{24}$$

If $\hat{\overline{\sigma}}_{\max} < 0$, the formula for meridians from the plastic condition has the following form:

$$\begin{aligned} \left(\frac{2}{3}\gamma + 1\right)\overline{q} - (\gamma + 3\alpha)\overline{p} &= (1-\alpha)\overline{\sigma}_c \qquad \text{(TM)}, \\ \left(\frac{1}{3}\gamma + 1\right)\overline{q} - (\gamma + 3\alpha)\overline{p} &= (1-\alpha)\overline{\sigma}_c \qquad \text{(CM)}. \end{aligned} \tag{25}$$

Assuming that:

$$K_c = \frac{\overline{q}_{(\mathrm{TM})}}{\overline{q}_{(\mathrm{CM})}}, \tag{26}$$

where $\overline{q}_{(\mathrm{TM})}$ and $\overline{q}_{(\mathrm{CM})}$ are the equivalent von Mises stresses determined for the meridians of tension and compression, respectively:

$$K_C = \frac{\gamma + 3}{2\gamma + 3}. \tag{27}$$

Ultimately, the formula is as follows:

$$\gamma = \frac{3\left(1 - K_c\right)}{2K_c - 1}. \tag{28}$$

When $\hat{\overline{\sigma}}_{\max} > 0$, the system of equations takes the following form:

$$\begin{aligned} \left(\frac{2}{3}\beta + 1\right)\overline{q} - (\beta + 3\alpha)\overline{p} &= (1-\alpha)\overline{\sigma}_c \quad \text{(TM)}, \\ \left(\frac{1}{3}\beta + 1\right)\overline{q} - (\beta + 3\alpha)\overline{p} &= (1-\alpha)\overline{\sigma}_c \quad \text{(CM)}. \end{aligned} \tag{29}$$

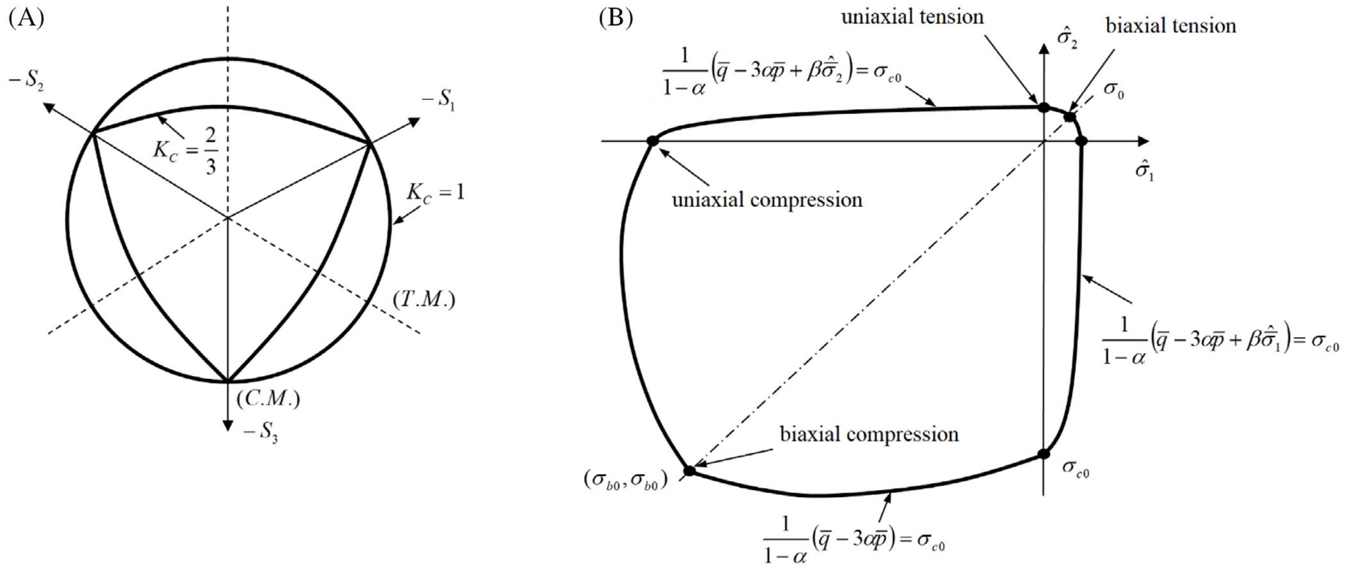

FIGURE 5 Plasticity area on the deviator plane depending on the parameter value K_c

Assuming that

$$K_t = \frac{\bar{q}_{(\mathrm{TM})}}{\bar{q}_{(\mathrm{CM})}}. \tag{30}$$

The formula takes the following form:

$$K_T = \frac{\beta + 3}{2\beta + 3}. \tag{31}$$

Figure 5 shows the plasticity area of the CDP model on the deviator plane.

In the damaged-plastic model, the non-associated law of flow was used:

$$\dot{\varepsilon}^{\mathrm{pl}} = \dot{\lambda}\frac{\partial G(\bar{\sigma})}{\partial \bar{\sigma}}. \tag{32}$$

In this formula, the plastic potential G in the form of a hyperbolic Drucker–Prager function was applied:

$$G = \sqrt{(\epsilon\sigma_{t0}\tan\psi)^2 + \bar{q}^2} - \bar{p}\tan\psi, \tag{33}$$

where ψ is the dilation angle in the p-q plane, σ_{t0} is the stress accompanying failure during uniaxial stretching, and ϵ is the eccentric distance of the function from its asymptote.

Continuity and smoothness are two features of a function that are important for determining the direction of the potential. The function in the zone of high closing pressure aims to achieve a linear form of the Drucker–Prager plastic potential and intersects the hydrostatic axis at an angle of 90°.

3.3 Load modeling

In the damaged-plastic model, damage is represented by reduction in the initial modulus of elasticity E_0 as a result of the introduction of scalar variable degradation:

$$E = (1 - d)E_0, \tag{34}$$

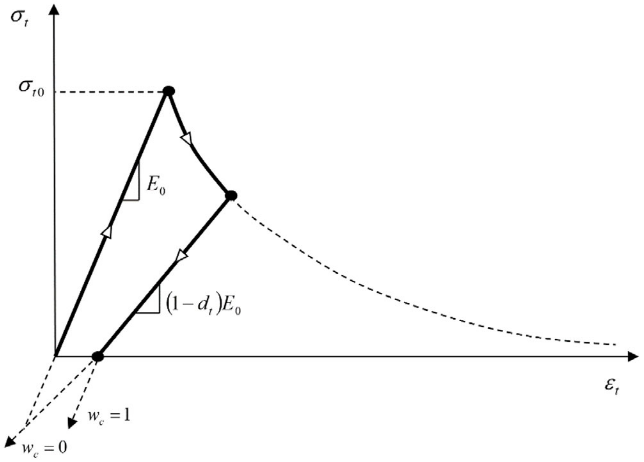

FIGURE 6 The effect of regaining the stiffness in compression by using the parameter w_c

where d is a function of the stress state and the uniaxial damage variables d_t and d_c. During cyclic loading in a uniaxial state, the equation has the following form:

$$(1-d) = (1-s_t d_c)(1-s_c d_t), \quad 0 \leq s_t, \quad s_c \leq 1, \tag{35}$$

where s_t and s_c are stress state functions that show the effect of regaining stiffness when changing the sign of stress:

$$\begin{aligned} s_t &= 1 - w_t r^* \left(\overline{\sigma}_{11}\right), 0 \leq w_t \leq 1, \\ s_c &= 1 - w_c \left(1 - r^* \left(\overline{\sigma}_{11}\right)\right), 0 \leq w_c \leq 1, \end{aligned} \tag{36}$$

where

$$r^* \left(\overline{\sigma}_{11}\right) = H\left(\overline{\sigma}_{11}\right) = \begin{cases} 1, & \overline{\sigma}_{11} > 0 \text{ (tension)}, \\ 0, & \overline{\sigma}_{11} < 0 \text{ (compression)}, \end{cases} \tag{37}$$

whereas w_t and w_c denote weight factors or tensile and compression stiffness recovery parameters that are related to material properties controlling stiffness recovery (Figure 6).

When changing the direction of the load from tensile to compressive (assuming that the material was not previously subjected to compression that would crush it $\tilde{\varepsilon}_c^{\text{pl}} = 0$ and d_c), the following equation was obtained:

$$(1-d) = (1-s_t d_c) = (1-(1-w_c(1-r^*))\, d_t). \tag{38}$$

In the case of tension, $\left(\overline{\sigma}_{11} > 0\right) r^* = 1$ and $d = d_t$. In the case of compression, $\left(\overline{\sigma}_{11} < 0\right) r^* = 0$ and $d = (1-w_c)\, d_t$. If $w_c = 1$, then $d = 0$, which means that the material has completely regained its stiffness $E = E_0$. On the other hand, if $w_c = 0$, then $d = d_t$ and there has been no recovery of stiffness. The values of w_c in the range of (0, 1) correspond to a partial recovery of stiffness.

The equations determining the development of equivalent plastic deformations for a uniaxial load are as follows:

$$\begin{aligned} \dot{\tilde{\varepsilon}}_t^{\text{pl}} &= r^* \dot{\varepsilon}_{11}^{\text{pl}}, \\ \dot{\tilde{\varepsilon}}_c^{\text{pl}} &= -(1-r^*)\, \dot{\varepsilon}_{11}^{\text{pl}}. \end{aligned} \tag{39}$$

For a unit phase of the cycle (tension / compression), they simplify to:

$$\begin{aligned} \dot{\tilde{\varepsilon}}_t^{\text{pl}} &= \dot{\varepsilon}_{11}^{\text{pl}}, \\ \dot{\tilde{\varepsilon}}_c^{\text{pl}} &= -\dot{\varepsilon}_{11}^{\text{pl}}. \end{aligned} \tag{40}$$

By analyzing complex multi-axial states, the above equation can be transformed to the following form:

$$\begin{aligned} \dot{\tilde{\varepsilon}}_t^{\mathrm{pl}} &= r(\hat{\bar{\boldsymbol{\sigma}}})\dot{\hat{\varepsilon}}_{\mathrm{max}}^{\mathrm{pl}}, \\ \dot{\tilde{\varepsilon}}_c^{\mathrm{pl}} &= -(1 - r(\hat{\bar{\boldsymbol{\sigma}}}))\dot{\hat{\varepsilon}}_{\mathrm{min}}^{\mathrm{pl}}, \end{aligned} \tag{41}$$

where $\dot{\hat{\varepsilon}}_{\mathrm{max}}^{\mathrm{pl}}$ and $\dot{\hat{\varepsilon}}_{\mathrm{min}}^{\mathrm{pl}}$ are the maximum and minimum eigenvalues of the plastic strain rate tensor $\dot{\varepsilon}^{\mathrm{pl}}$, while $r(\hat{\bar{\boldsymbol{\sigma}}})$ is the stress weighting factor:

$$r(\hat{\bar{\boldsymbol{\sigma}}}) = \frac{\sum_{i=1}^{3} \left\langle \hat{\bar{\sigma}}_i \right\rangle}{\sum_{i=1}^{3} \left| \hat{\bar{\sigma}}_i \right|}, \quad 0 \leq r(\hat{\bar{\boldsymbol{\sigma}}}) \leq 1. \tag{42}$$

The weighting factor is 1 if all principal stresses are positive, and it is 0 if they are negative:

$$\langle x \rangle = \frac{1}{2}(|x| + x). \tag{43}$$

When the eigenvalues of the plastic strain rate tensor $\dot{\hat{\varepsilon}}_i$ $(i = 1, 2, 3)$ satisfy the relationship:

$$\dot{\hat{\varepsilon}}_{\mathrm{max}}^{p\mathrm{l}} = \dot{\hat{\varepsilon}}_1 \geq \dot{\hat{\varepsilon}}_2 \geq \dot{\hat{\varepsilon}}_3 = \dot{\hat{\varepsilon}}_{\mathrm{min}}^{\mathrm{pl}}. \tag{44}$$

The equation for the general complex state is given by the formula:

$$\dot{\hat{\varepsilon}}^{\mathrm{pl}} = \begin{bmatrix} \dot{\hat{\varepsilon}}_t^{\mathrm{pl}} \\ \dot{\hat{\varepsilon}}_c^{\mathrm{pl}} \end{bmatrix} = \hat{\boldsymbol{h}}\left(\hat{\bar{\boldsymbol{\sigma}}}, \tilde{\varepsilon}^{\mathrm{pl}}\right) \cdot \tilde{\varepsilon}^{\mathrm{pl}}, \tag{45}$$

where

$$\hat{\boldsymbol{h}}\left(\hat{\bar{\boldsymbol{\sigma}}}, \tilde{\varepsilon}^{\mathrm{pl}}\right) = \begin{bmatrix} r(\hat{\bar{\boldsymbol{\sigma}}}) & 0 & 0 \\ 0 & 0 & -(1 - r(\hat{\bar{\boldsymbol{\sigma}}})) \end{bmatrix}, \tag{46}$$

$$\dot{\hat{\varepsilon}}^{\mathrm{pl}} = \begin{bmatrix} \dot{\hat{\varepsilon}}_1^{\mathrm{pl}} \\ \dot{\hat{\varepsilon}}_2^{\mathrm{pl}} \\ \dot{\hat{\varepsilon}}_3^{\mathrm{pl}} \end{bmatrix}. \tag{47}$$

Stiffness degradation in the damaged-plastic model is created using a single isotropic degradation variable d:

$$\boldsymbol{D}^{\mathrm{el}} = (1 - d)\boldsymbol{D}_0^{\mathrm{el}}, \quad 0 \leq d \leq 1. \tag{48}$$

The variable d reflects the degradation mechanism during cyclic loading, and at the same time it must be consistent with the above-mentioned response of the material under monotonic loading:

$$(1 - d) = (1 - s_t d_c)\,(1 - s_c d_t)\,, \quad 0 \leq s_t, \quad s_c \leq 1. \tag{49}$$

It can be seen that the equation is similar to the description for a uniaxial cyclic load. The only difference is that the parameters s_t and s_c are expressed using functions $r(\hat{\bar{\boldsymbol{\sigma}}})$:

$$\begin{aligned} s_t &= 1 - w_t\, r(\hat{\bar{\boldsymbol{\sigma}}}), \quad 0 \leq w_t \leq 1, \\ s_c &= 1 - w_c(1 - r(\hat{\bar{\boldsymbol{\sigma}}})), \quad 0 \leq w_c \leq 1. \end{aligned} \tag{50}$$

The results obtained from the experimental tests of quasi-brittle materials confirm the phenomenon of the recovery of stiffness, which consists in the closing of cracks when the direction of the load changes from tension to compression.

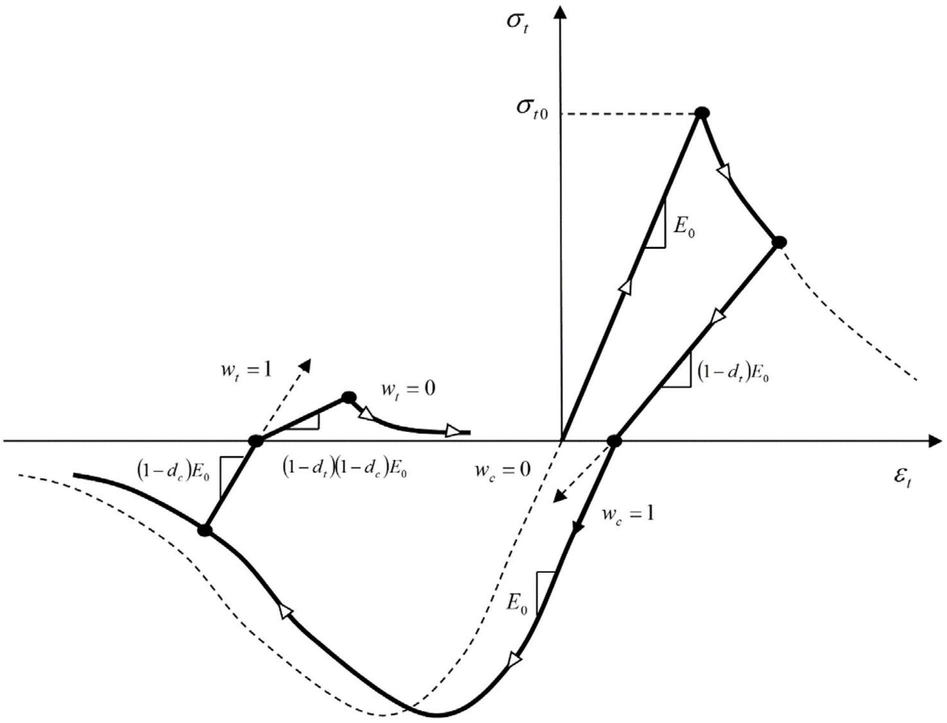

FIGURE 7 Uniaxial cycle of tension–compression–tension

On the other hand, stiffness will not be recovered when the direction of the compressive and tensile load changes, but the microcracking process has started in the material under the influence of crushing. This corresponds to the values of $w_t = 1$ and $w_c = 1$.

The essence of the plastic-degradation model is to define the mechanism of concrete destruction in single-axis conditions, followed by the correct transfer of this mechanism into more complex, multi-axis conditions. Below, we present the algorithms for the implementation of local and non-local models for the elastic–plastic laws, which relate to both the Drucker–Prager criterion and the “elastic–plastic” degradation law. The χ symbol used in this chapter shall be the parameter of amplification/deficiency, κ_1 for the Drucker–Prager criterion and the pseudo-logarithmic degradation parameter L related to the degradation law (Figure 7).

3.4 | Implementation of the local model

In this article, a return mapping algorithm was used to implement the local model. According to this method, in a given computational iteration, at the first computational stage, it is assumed that the whole increase in deformation is elastic $\Delta\varepsilon \rightarrow \Delta\varepsilon^e$. Next, trial stresses are calculated for the assumed deformations.

$$\boldsymbol{\sigma}^{\text{trial}} = \Delta\boldsymbol{R}\boldsymbol{\sigma}^t\Delta\boldsymbol{R}^T + \boldsymbol{C} : \Delta\varepsilon, \tag{51}$$

where $\Delta\boldsymbol{R}$ determines the increment of the stiff-rotation tensor (Hughes–Winget).

$$\Delta\boldsymbol{R} = \left(\boldsymbol{I} - \frac{1}{2}\Delta\boldsymbol{\omega}\right)^{-1}\left(\boldsymbol{I} - \frac{1}{2}\Delta\boldsymbol{\omega}\right). \tag{52}$$

In the equation above, $\Delta\boldsymbol{\omega}$ is the increment of the spin tensor

$$\Delta\boldsymbol{\omega} = \text{asym}\left(\frac{\partial\Delta\boldsymbol{u}}{\partial\boldsymbol{x}^{t+\Delta t/2}}\right). \tag{53}$$

If small displacements and deformations are assumed, the increment of the rigid rotation tensor is a unit tensor ($\Delta\boldsymbol{R} = \boldsymbol{I}$). The stiffness tensor $\boldsymbol{C}$ in Equation (51), respectively means the initial stiffness tensor $\boldsymbol{C}^{\text{e}}$ for the Drucker–Prager criterion and the secant stiffness tensor $\boldsymbol{C}^s$ for the degradation law. At the same time, in the second model, the secant stiffness tensor also changes due to increased degradation. Thus, formally, the stress increment, in this case, is equal to

$$\Delta\boldsymbol{\sigma} = \left(\boldsymbol{C}^s\right)^{t+\Delta t} : \Delta\varepsilon + \left(\left(\boldsymbol{C}^s\right)^{t+\Delta t} - \left(\boldsymbol{C}^s\right)^{t}\right) : \varepsilon^{t}. \tag{54}$$

If at the end of the increment the $f\left(\boldsymbol{\sigma}, \chi^t\right) \leq 0$ condition is met, then the computed stresses $\boldsymbol{\sigma}^{\mathrm{trial}}$ are assumed to be the values at the end of the increment $\boldsymbol{\sigma}^{\mathrm{trial}} \rightarrow \boldsymbol{\sigma}^{t+\Delta t}$. Otherwise, the stresses are corrected. The stresses are brought back to the plasticity plane. Therefore, we strive to meet the condition $f\left(\boldsymbol{\sigma}^{t+\Delta t}, \chi^{t+\Delta t}\right) = 0$.

To solve the system of equations (55)–(57)

$$\boldsymbol{\sigma}^{t+\Delta t} = \Delta\boldsymbol{R}\boldsymbol{\sigma}^{t}\Delta\boldsymbol{R}^{T} + \boldsymbol{C} : \left(\Delta\varepsilon - \Delta\varepsilon^{p,d}\right), \tag{55}$$

$$\Delta\varepsilon^{p,d} = \Delta\lambda \left.\frac{\partial g}{\partial\boldsymbol{\sigma}}\right|_{t+\Delta t}, \tag{56}$$

$$\chi^{t+\Delta t} = \chi^{t} + \Delta\chi, \quad \Delta\chi = \eta\Delta\lambda. \tag{57}$$

We used a cutting plane algorithm as proposed by Simo and Ortiz.[30,31] The $\Delta\varepsilon^{p,d}$ symbol is the plastic deformation $\Delta\varepsilon^{p}$ or deformation related to degradation $\Delta\varepsilon^{d}$ according to the analyzed material law. Assuming the following quantities

$$\chi^{(0)} = \chi^{(t)}, \left(\Delta\varepsilon^{p,d}\right)^{(0)} = \left(\Delta\varepsilon^{p,d}\right)^{(t)}, \boldsymbol{\sigma}^{(0)} = \boldsymbol{\sigma}^{\mathrm{trial}}, f^{(0)} = f\left(\boldsymbol{\sigma}^{(0)}, \chi^{(0)}\right). \tag{58}$$

An expression for change (correction) of deformations is received

$$\delta\varepsilon^{p,d} = \delta\lambda\left(\frac{\partial g}{\partial\boldsymbol{\sigma}}\right)^{(i)}. \tag{59}$$

Together with change (correction) of the plastic factor

$$\delta\lambda = \frac{f\left(\boldsymbol{\sigma}^{(i)}, \chi^{(i)}\right)}{\left(\frac{\partial f}{\partial\sigma}\right)^{(i)} : \boldsymbol{C} : \left(\frac{\partial g}{\partial\sigma}\right)^{(i)} - \left(\eta\frac{\partial f}{\partial\chi}\right)^{(i)}}. \tag{60}$$

The $\delta(\bullet)$ symbol in Equations (59) and (60) means a change in a given quantity between successive iterations. The plastic factor and the reinforcement/degradation parameter are updated according to the following dependencies

$$\Delta\lambda^{(i+1)} = \Delta\lambda^{(i)} + \delta\lambda, \chi^{(i+1)} = \chi^{(i)} + \delta\eta\lambda^{(i)}, \tag{61}$$

whereas for the stress it is

$$\boldsymbol{\sigma}^{(i+1)} = \boldsymbol{\sigma}^{(i)} - \delta\lambda\boldsymbol{C} : \left(\frac{\partial g}{\partial\boldsymbol{\sigma}}\right)^{(i)}. \tag{62}$$

For the degradation law, instead of formula (62), the stresses at the end of a given increment can be determined directly from the updated stiffness tensor and total strain tensor (Equation (NR)). In addition, the following conditions must be met in an iterative process

$$\Delta\lambda^{(i+1)} \geq 0, \chi^{(i+1)} \geq \chi^{(0)}. \tag{63}$$

The iteration process ends when the convergence condition is met

$$\left|f^{(i)}\right| \leq Tr^{(0)}, \tag{64}$$

where T is the adopted tolerance and $r^{(0)}$ is the material response to the parameters at the beginning of the iteration process. The tolerance assumed in the simulations was $T = 10^{-6}$.

The relationship (60) for the Drucker–Prager condition is

$$\delta\lambda_1 = \frac{f_1\left(\boldsymbol{\sigma}^{(i)}, \kappa_1^{(i)}\right)}{3G - K\tan\beta\tan\psi + H_1^{(i)}A_1}, \tag{65}$$

where

$$H_1 = \frac{d\sigma_c(\kappa_1)}{d\kappa_1}, \quad \text{oraz} A_1 = \left(1 - \frac{1}{3}\tan\beta\right)\left(1 - \frac{1}{3}\tan\psi\right) \tag{66}$$

Invariants are updated according to the formulas:

$$q^{(i)} = q^{\text{trial}} - 3G\Delta\lambda_1^{(i)}, \quad p^{(i)} = p^{\text{trial}} - K\tan\psi\Delta\lambda_1^{(i)} \tag{67}$$

Due to the fact that the invariant q must be non-negative, the maximum value of the plastic factor must not exceed

$$\Delta\lambda_{\max} = \frac{q^{\text{trial}}}{3G}. \tag{68}$$

Change in the increment parameter at the end of each increment is

$$\kappa_1^{t+\Delta t} = \kappa_1^{t} + \left(1 - \frac{1}{3}\tan\beta\right)\frac{f^{\text{trial}} - 3G\Delta\lambda_{\max}}{K(\tan\beta)^2}, \tag{69}$$

whereas elastic and plastic deformations are updated according to the following relationships

$$\left(\varepsilon^{e}\right)^{t+\Delta t} = \frac{\left(1 - \frac{1}{3}\tan\beta\right)\frac{\sigma_c\left(\kappa_1^{t+\Delta t}\right)}{\tan\beta}}{3K}\boldsymbol{I}, \tag{70}$$

$$\left(\varepsilon^{P}\right)^{t+\Delta t} = (\varepsilon)^{t} + (\Delta\varepsilon)^{t+\Delta t} - \left(\varepsilon^{e}\right)^{t+\Delta t}. \tag{71}$$

For the law with a degradation surface taking the form of an elastic–plastic condition, the correction for the plastic multiplier of Equation (50) is

$$\delta\lambda_L = \frac{\sum_{k=1}^{3}\frac{1}{2}\left\langle \tilde{\sigma}_{(k)}^{(i)} \right\rangle \left\langle \tilde{\varepsilon}_{(k)}^{(i)} \right\rangle - r\left(L^{(i)}\right)}{\sum_{k=1}^{3}\frac{1}{2}\left\langle \tilde{\sigma}_{(k)}^{(i)} \right\rangle \left\langle \tilde{\varepsilon}_{(k)}^{(i)} \right\rangle - r\left(L^{(i)}\right) + H_L^{(i)}}, \tag{72}$$

where

$$H_L = \frac{dr(L)}{dL}. \tag{73}$$

Change of the degradation parameter at the end of each increment is equal to

$$L^{t+\Delta t} = L^{t} + \eta\Delta\lambda_L. \tag{74}$$

The secant stiffness module in the current increment can be calculated as

$$\left(\boldsymbol{C}^{S}\right)^{t+\Delta t} = \exp\left(-L^{t+\Delta t}\right)\boldsymbol{C}^{e}. \tag{75}$$

Ultimately, the current stress at the end of a given increment, taking into account the increase in degradation, can be determined according to the formula

$$\boldsymbol{\sigma}^{t+\Delta t} = \left(\boldsymbol{C}^{s}\right)^{t+\Delta t}(\varepsilon)^{t+\Delta t}. \tag{76}$$

3.5 | Implementation of the non-local model

The implementation of non-local models, in addition to the general plasticity algorithms presented in the previous section, also requires consideration of non-local theory. It is necessary to apply additional operations on algorithms allowing for proper implementation of non-local procedures.

Equation (60) after transformations can be written as

$$f\left(\boldsymbol{\sigma}^{(i)}, \chi^{(i)}\right) - \frac{1}{\eta}\left(\frac{\partial f}{\partial \boldsymbol{\sigma}}\right)^{(i)} : C : \left(\frac{\partial g}{\partial \boldsymbol{\sigma}}\right)^{(i)} \delta\chi - \left(\frac{\partial f}{\partial \chi}\right)^{(i)} \delta\chi = 0. \tag{77}$$

After introducing additional markings

$$f^{\text{trial}} = f\left(\boldsymbol{\sigma}^{(i)}, \chi^{(i)}\right), M^{(i)} = \frac{1}{\eta}\left(\frac{\partial f}{\partial \boldsymbol{\sigma}}\right)^{(i)} : \boldsymbol{C} : \left(\frac{\partial g}{\partial \boldsymbol{\sigma}}\right)^{(i)} \delta\chi, H^{(i)} = \left(\frac{\partial f}{\partial \chi}\right)^{(i)}. \tag{78}$$

Equation (77) takes the form

$$f^{\text{trial}} - M^{(i)}\Delta\chi - H^{(i)}\Delta\chi = 0, \tag{79}$$

where $\Delta\chi$ is the increment of parameter χ in a given step. For the Drucker–Prager criterion, non-locality is introduced using the definition provided by Brinkgreve[32] and Vermeer and Brinkgreve[33]

$$\hat{\kappa}(x) = (1-m)\kappa(x) + m\overline{\kappa}(x) \Rightarrow \hat{\kappa}(x) = (1-m)\kappa(x) + m\int_V \alpha(x,\xi)\kappa(\xi)d(\xi). \tag{80}$$

We thus receive

$$f\left(\boldsymbol{\sigma}^{t+\Delta t}, \hat{\kappa}^{t+\Delta t}\right) = 0 \tag{81}$$

and Equation 79 taking into account the non-local reinforcement parameter

$$f^{\text{trial}} - M^{(i)}\Delta\kappa - H^{(i)}\Delta\hat{\kappa} = 0. \tag{82}$$

In a general case, in this equation, the increment in the non-local gain parameter is

$$\Delta\hat{\kappa}(\boldsymbol{x}) = (1-m)\Delta\kappa(\boldsymbol{x}) + m\int_V \alpha(\boldsymbol{x},\boldsymbol{\xi})\Delta\kappa(\boldsymbol{\xi})d(\boldsymbol{\xi}). \tag{83}$$

However, since it is assumed that non-locality can only be introduced in a weakened area (the local definition applies in the reinforcement area), it is necessary to modify Equation 83

$$\Delta\hat{\kappa}(\boldsymbol{x}) = \Delta\kappa(\boldsymbol{x}) + m\left(\int_v \alpha(\boldsymbol{x},\boldsymbol{\xi})\Delta\kappa^{\bullet}(\xi)d(\xi) - \Delta\kappa^{\bullet}(\boldsymbol{x})\right), \tag{84}$$

where the symbol $\Delta\kappa^{\bullet}$ stands for

$$\Delta\kappa^{\bullet}(\boldsymbol{x}) = \begin{cases} 0, & H(\boldsymbol{x}) \geq 0 \text{ reinforcement}, \\ \Delta\kappa(\boldsymbol{x}), & H(\boldsymbol{x}) < 0 \text{ weakening}. \end{cases} \tag{85}$$

Thus, the value of the parameter $\hat{\kappa}$ at the end of the increment, taking into account the conditions $\Delta\hat{\kappa} \geq 0$ and $\Delta\kappa \geq 0$ is equal to

$$\hat{\kappa}(\boldsymbol{x})^{t+\Delta t} = \hat{\kappa}(\boldsymbol{x})^{t} + \max\{0, (1-m)\Delta\kappa(\boldsymbol{x}) + m\Delta\kappa(\boldsymbol{x})\} = \hat{\kappa}(\boldsymbol{x})^{t} + \max\{0, \Delta\hat{\kappa}(\boldsymbol{x})\}. \tag{86}$$

When changing to the finite element method, the non-local gain parameter gain can be written as

$$\Delta\boldsymbol{\kappa} = \boldsymbol{A}\Delta\boldsymbol{\kappa}, \tag{87}$$

where $\boldsymbol{A}$ is a matrix of non-local coefficients, sized $N \times N$ (N being the number of integration points). Its terms are equal to

$$A_{kl} = \frac{\alpha_g \left(\left\| \boldsymbol{x}^k - \boldsymbol{x}^l \right\| \right) V \left(\boldsymbol{x}^l \right)}{\sum_{j=1}^{N} \alpha_g \left(\left\| \boldsymbol{x}^k - \boldsymbol{x}^j \right\| \right) V \left(\boldsymbol{x}^j \right)}, \tag{88}$$

where α_g is defined by the formula

$$\alpha_g = \frac{1}{c_1} \exp \left(-\frac{r^2}{l_c^2} \right). \tag{89}$$

By analogy, Equation 82, after discretization, takes the following form

$$\boldsymbol{f}^{\text{trial}} = \boldsymbol{M} \Delta \boldsymbol{\kappa} - (1 - m) \boldsymbol{H} \Delta \boldsymbol{\kappa} - m \boldsymbol{H} \boldsymbol{A} \Delta \boldsymbol{\kappa} \leq 0. \tag{90}$$

$\boldsymbol{M}$ and $\boldsymbol{H}$ diagonal matrices, respectively, contain M and H coefficients for all integration points. When only points in the plastification condition are taken into account, the inequality 90 takes the form

$$\boldsymbol{f}^{\text{trial}} = \boldsymbol{B} \Delta \boldsymbol{\kappa}, \tag{91}$$

where $\boldsymbol{B}$ is equal to

$$\boldsymbol{B} = \boldsymbol{M} + (1 - m) \boldsymbol{H} + m \boldsymbol{H} \boldsymbol{A}. \tag{92}$$

Numerical solution to system (91) is usually based on the division of the $\boldsymbol{B}$ matrix into two matrices, one of which is easy to reverse. Among others, such methods have been presented by Benvenuti and Trali,[34] and Stromberg and Ristinmaa.[35] The iterative solving process ends when the following conditions are met

$$f \left(\boldsymbol{\sigma}^{t+\Delta t}, \kappa^t + \Delta \hat{\kappa} \right) \leq 0, \Delta \kappa^{(i+1)} = 0, \tag{93}$$

for all points in the elastic area, and

$$\left\| f \left(\boldsymbol{\sigma}^{t+\Delta t}, \kappa^t + \Delta \hat{\kappa} \right) \right\| \leq Tr^{(i=0)}, \quad \Delta \kappa^{(i+1)} > 0, \tag{94}$$

for the points in the plastification area.

The basic difficulty in the described method lies in the necessity to determine the non-local reinforcement parameter 86 in each iteration and at all points. Another problem is related to the need to perform calculations simultaneously for all points of integration in the model.

For the Drucker–Prager criterion, the increment estimation $\Delta\kappa$, proposed by Brinkgreve,[32] was used. Approximate values of increments of the reinforcement parameter $\Delta\kappa^*$ were determined on the basis of increments of the total strain tensor

$$\Delta \kappa^* = \left(1 - \frac{1}{3} \tan \psi \right) \sqrt{\frac{2}{3} \Delta e : e}. \tag{95}$$

As a result, the approximate increase in the non-local increment parameter for a fixed integration point is equal to

$$\Delta \hat{\kappa}^* = \Delta \kappa + m \left(\boldsymbol{\alpha} \Delta \boldsymbol{\kappa}^* - \Delta \kappa^* \right), \tag{96}$$

where $\boldsymbol{\alpha}$ means a row in the $\boldsymbol{A}$ matrix corresponding to a given integration point. In addition, condition (81) takes the form

$$f \left(\boldsymbol{\sigma}^{t+\Delta t}, \kappa^t + \Delta \hat{\kappa}^* \right) = 0, \tag{97}$$

which means that in the point under consideration (in a given time increment) only the value of the increment $\Delta\kappa$ changes, while the influence of neighboring points remains constant. It is therefore possible to solve Equation 97 in the same way as for local plasticity.

To determine the non-local energy value in a given iteration, a mixed formulation based on known local and non-local energy values determined in the given iteration and in the previous iteration were used, see Stromberg and Ristinmaa[35] and Zhang et al.[36]

$$\left(\overline{Y}^{*}\right)^{(i)} = (1 - m + mA_{kl})\, Y^{(i)} + m\left(\overline{Y}^{(i-1)} - Y^{(i-1)}A_{kl}\right). \tag{98}$$

4 | IMPLEMENTATION OF NONLOCAL DAMAGE INTEGRAL REGULARIZATION

4.1 | Constitutive integration: solution algorithm at the integration point level

For the implementation of the programme we used, among others, the *UMAT* and *UEL* user subprocedures. These procedures allow for extending the capabilities of the programme using the FORTRAN language. The user can modify subprocedures within specific templates (i.e., to ensure their compatibility with the whole programme). It is necessary to define specific output quantities (vectors, matrices, etc.) transmitting the necessary information to the computation solver. The *UMAT* procedure allows the user to define his or her material rights at integration points. For given $\boldsymbol{\sigma}^t$, ε^t, $\Delta\boldsymbol{\sigma}$ the procedure requires the determination of the stresses $\boldsymbol{\sigma}^{t+\Delta t}$ and the stiffness matrix $\mathbf{C}$. The UEL procedure allows the user to define his or her own elements. For given displacements $\boldsymbol{u}^t$, known increments of $\Delta\boldsymbol{u}$ displacements, and the adopted constitutive law, it is necessary to determine the vector of near-node forces, and the element's stiffness matrix.

Basic information that is needed in each of the described non-local algorithms includes components of the non-local matrix $\boldsymbol{A}$. Therefore, it is necessary to gather information about integration coordinate points $\boldsymbol{x}^{\mathrm{IP}}$ and volumes V^{IP} associated with these points. In the analysis if large displacements are assumed, these values change in each iteration. However, when assuming small displacements, $\boldsymbol{x}^{\mathrm{IP}}$ and V^{IP} remain constant throughout the entire straining process. As the required data is not available in the Abaqus software, it is necessary to collect the data by ourselves. *UEL* or *UMAT* procedures can be used for this purpose. In the first case, it is necessary to use an additional finite element grid only intended for data collection. This grid has the same nodes and edges as the base grid. For such a grid, we need to define coordinates of the points of integration $\boldsymbol{x}^{\mathrm{IP}}$ and V^{IP} volumes. We may also determine the strain increments $\Delta\varepsilon$, which will later be used to calculate approximations (e.g., in the Brinkgreve method). For the *UMAT* procedure, the $\boldsymbol{x}^{\mathrm{IP}}$ and $\Delta\varepsilon$ values are known as input values in each iteration. By contrast, the so-called characteristic element length l_{el}, available in this procedure, can be used to determine the V^{IP} volume. This value has nothing in common with the characteristic microstructure length l_c. It is defined as a second (or third) degree root of the field (or volume) of a finite element. The results obtained using the *UMAT* and *UEL* procedures are only identical for elements with one integration point. If there are multiple integration points, minor differences may arise between the determined volumes associated with the integration points.

Another problem results from the fact that after executing the *UEL* or *UMAT* procedure, the user only has access to information related to a given integration point. However, data on the remaining points is not accessible. This problem can be solved by using common memory areas employing the *COMMON* command. Data on coordinates of all $\boldsymbol{x}^{\mathrm{IP}}$ integration points, V^{IP} volumes, as well as other necessary information (e.g., $\Delta\kappa$, $\Delta\kappa^{*}$), degradation parameters L, effective strains $\tilde{\varepsilon}$, etc. are stored in declared and globally available data tables.

Two stages can be distinguished in the implementation of non-local algorithms. The first one is connected with collecting information from neighboring points, and the second one concerns the calculations themselves. Therefore, to update the strains, it is necessary to loop through all elements twice. Unfortunately, in Abaqus Standard, it is not possible to call *UEL* or *UMAT* procedures twice for the same point in one iteration. This problem can be resolved in two ways. The first consists of dividing the iteration into computational iterations and data collection iterations. In such a case, the stain is only updated during computational iteration. Therefore, no configuration change is required when switching from data collection iterations to computational iterations. For this purpose, it is essential to obtain a global system of equations in the form

$$\boldsymbol{K}\delta\boldsymbol{u} = \mathbf{0}. \tag{99}$$

To obtain vector $\mathbf{0}$ on the right, all stains must be zero. In addition, all external loads must be temporarily reset to zero. However, it may happen that the displacement convergence criteria are met and the solution of Equation (98) will be accepted. As a consequence, the transition to a new increment will take place. To prevent this, it must be impossible to complete the global iteration after the data collection iteration. For this purpose, in addition to the existing model, we defined an additional lattice element subjected to tension P. In the non-computational iterations, in such an element the node forces are equal to zero, while the external loads are not set to zero. This leads to a global system of equilibrium equations

$$\begin{bmatrix} \boldsymbol{K} & \boldsymbol{0} \\ \boldsymbol{0}^T & K_K \end{bmatrix} \begin{bmatrix} \delta \boldsymbol{u} \\ u_K \end{bmatrix} = \begin{bmatrix} \boldsymbol{0} \\ P \end{bmatrix}, \tag{100}$$

where K_K is the stiffness of the lattice element. With a sufficiently high value of force P assumed, the convergence criteria for the balance of forces are not met. However, the value of force P should not be too large to influence the value of the time-averaged force as little as possible $\tilde{q}$.

The second way is to use two lattices. A basic lattice for the determination of stresses, and an additional one, exclusively for data collection. Such an implementation method requires an appropriate order of calling the elements. First, all elements of the additional lattice should be called and then, once the necessary data is collected, the elements of the actual lattice.

Below, we present our algorithm that shows how degradation is calculated in each iteration step.

Algorithm 1. Non-local degradation model in the form of elastic–plastic law

1. Determination of the elastic stiffness matrix $\boldsymbol{C}^e$
2. Deformations at the beginning of the increment $(\varepsilon)^{t+\Delta t} = (\varepsilon)^t + \Delta\varepsilon$
3. Effective deformation $(\tilde{\varepsilon})^{t+\Delta t} = \exp\left(-L^2/2\right)(\varepsilon)^{t+\Delta t}$
4. Effective stresses $\tilde{\boldsymbol{\sigma}} = \boldsymbol{C}^e : (\tilde{\varepsilon})^{t+\Delta t}$
5. Determination of the non-local elastic deformation energy $\overline{Y}^*$ from Equation (98)
6. Checking for plastification $f\left(\overline{Y}^*\right) - r\left(L^{t+\Delta t}\right) \geq 0$
7. If condition (56) is met:

a) initialization: $f^{(0)} = f\left(\overline{Y}^*\right), \quad \Delta L^{(0)} = 0, \quad i = 0$

b) calculating correction δL (Equation 72) and updating of the increment $\Delta L^{(i+1)}$ calculating correction $\delta\lambda$ (Equation 60) and updating $\Delta\kappa^{(i+1)}$ calculation of the non-local reinforcement parameter $\left(\Delta\hat{\kappa}^*\right)^{(i+1)}$ (Equation 96)

c) update of the load function $f\left(\overline{Y}^*\right)^{(i+1)}$

d) verification of the convergence condition $\left| f\left(\overline{Y}^*\right)^{(i+1)} - r\left(L^t + \Delta L^{(i+1)}\right) \right| \leq Tr^{(0)}$

8. If condition (7d) is met: stress update $\boldsymbol{\sigma}^{t+\Delta t}$ (Equation 76) or determination of strains $(\varepsilon^e)^{t+\Delta t}$ and $(\varepsilon^p)^{t+\Delta t}$ (Equations 70 and 71), otherwise, return to point (7b)
9. If condition (6) is not met: $L^{t+\Delta t} = L^t$
10. Implementation of: elastic–plastic model's parameters with stiffness degradation that characterize the plastic deformations emergence, variable compressive and tensile deformation, and the ones that can simulate the *stiffness recovery effect*—according to the Appendix

---

5 MODEL VALIDATION

5.1 Axially compressed component

To verify the correctness of the adopted Algorithm 1, a plastic-degradation model of concrete was validated with an axially compressed element. We analyzed a concrete element sized 400 × 100 mm^2, its geometry is shown in Figure 8. Due to the specific character of the research problem (analysis of nonlinear material under cyclic load), generating a significant number of equations for each increment, a 2D analysis was carried out in this case. At the element base, at the point lying on the axis of symmetry, we blocked horizontal shift and vertical shift. The possibility of horizontal displacement was also blocked for the remaining nodes located on the bottom of the analyzed element (Figure 8).

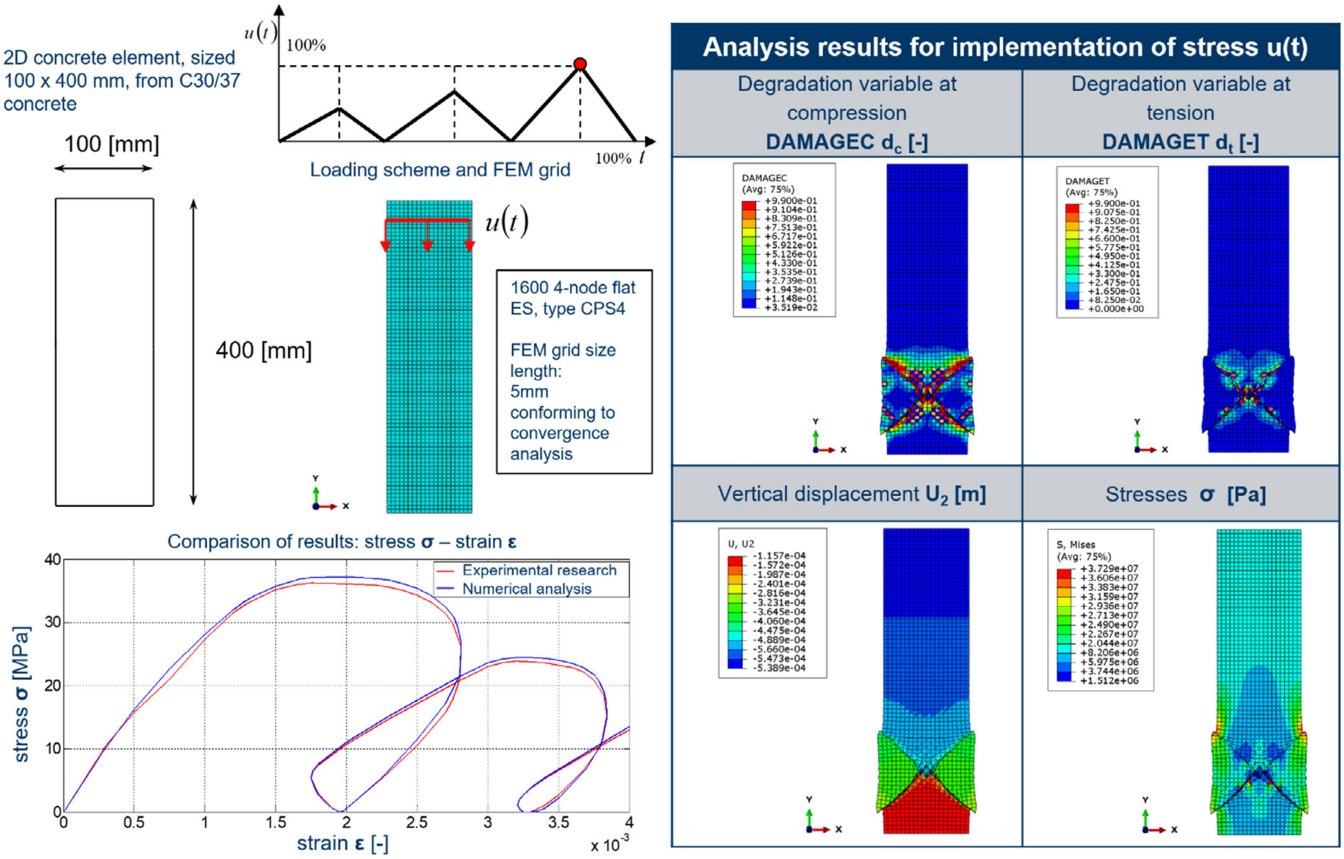

FIGURE 8 Validation of the CDP model with an axially compressed component

The element was divided into 1600 flat (2D) continuous four-node CPS4 type finite elements with a bilateral shape function. There were 1701 nodes in total. The calculations were performed for several finite element grid sizes. The greatest convergence was obtained for a grid with a side length of 5 mm. The convergence criterion assumed for defining the best mesh discretization was adopted based on displacement at point. The grid size was considered correct when the difference in the displacement results at the point between the two grid pitch sizes was approx. 2%.

The load was modeled kinematically as an equal vertical displacement of the upper element surface nodes. In the numerical simulation, we used concrete with compressive strength of $\boldsymbol{f_c} = \mathbf{37\ MPa}$. All necessary material characteristics were obtained based on the parameters given in the Appendix. The degradation calculation procedure in each iteration step was implanted as presented in Algorithm 1.

Below, we present selected results obtained during the simulation. They relate to the end of the simulation (last increment).

Calibration of the plastic-degradation model implemented in the ABAQUS program allowed prediction of element scratching, and the stresses and deformations (including plastic ones) accompanying it. Moreover, it allowed for observing the progressive material degradation under cyclic load. Figure 8 shows subsequent, bending loops of the relief-load hysteresis. The results obtained are consistent with the trends presented in the literature and are promising with respect to using this model to simulate cyclic loading.

5.2 | Three-point bending test

Once Algorithm 1 was correctly validated on a compressed element, we proceeded to checking its correctness with a bent element. Concrete tensile behavior modeling is very important for a realistic representation of a structural element's work. We analyzed a $100 \times 100 \times 450\ \text{mm}^3$ concrete element based on symmetrical hinged and non-sliding supports. In the middle of the element's span, a 2 mm wide and 20 mm deep notch was made from underneath. A load was applied to

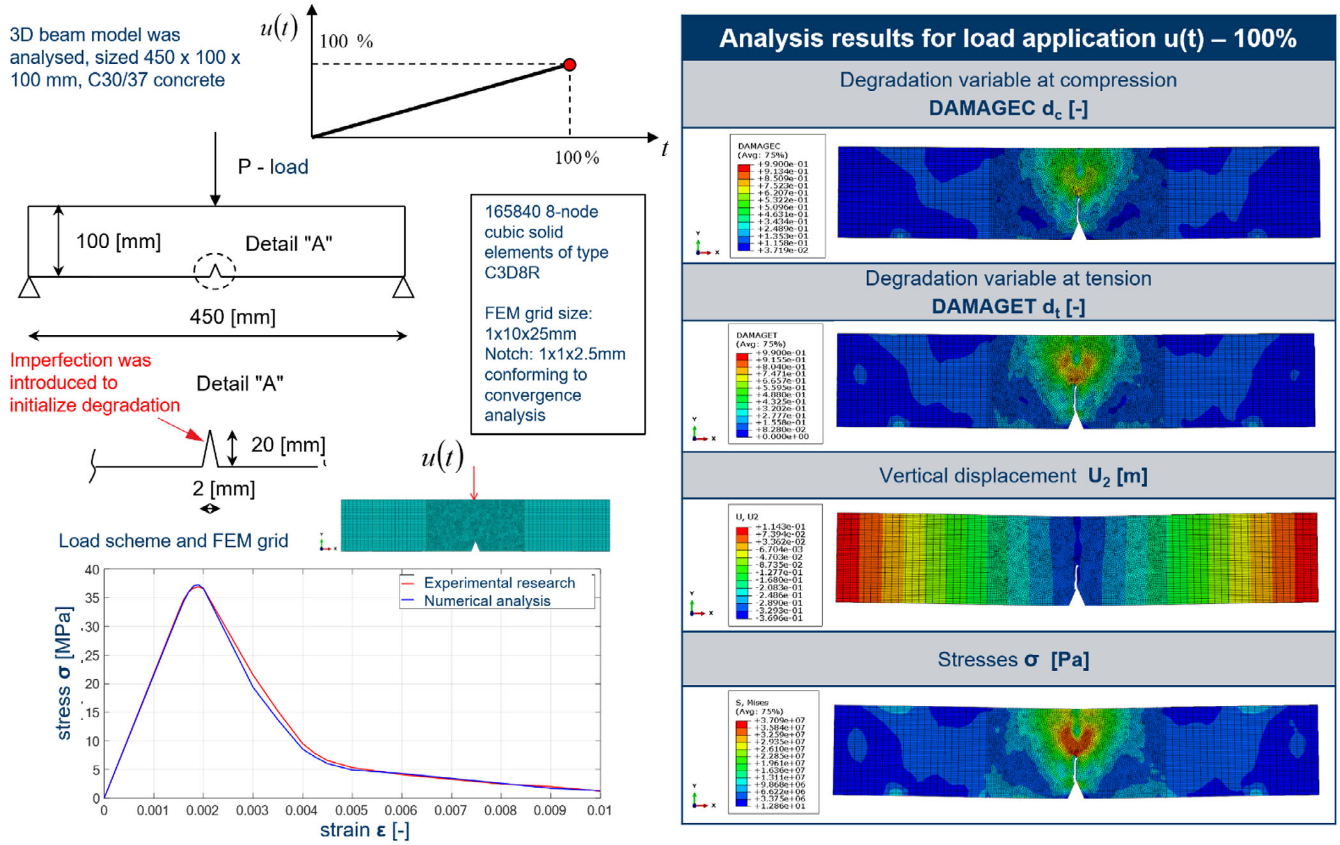

FIGURE 9 Validation of CDP model with a three-point-bent element

the upper surface of the element (on the extension of the notch axis). The geometry is schematically presented in Figure 9. We aimed to determine the place and extent of the scratched area in the analyzed element created under the load (i.e., the so-called three-point bending).

The beam was divided into 165,840 eight-node solid cubic elements of reduced integration, with a linear shape function of type C3D8R, with a total number of 211,656 nodes. The size of the finite element grid for which the greatest convergence was obtained was $1 \times 10 \times 25\,\text{mm}^3$. The convergence criterion assumed for defining the best mesh discretization was adopted based on displacement at point. The grid size was considered correct when the difference in the displacement results at the point between the two grid pitch sizes was approx. 2%. In the notch area, the finite element grid was denser to obtain a more accurate result. The denser area was a 25 mm wide band, where $1 \times 1 \times 25\,\text{mm}^3$ elements were used (Figure 9).

The load amplitude in the vertical axis was 13.8 kN, and during the numerical simulation, the load was applied over the entire section width.

For numerical calculations, we used concrete with a compressive strength of $\boldsymbol{f_c = 37}$ **MPa.** All necessary material characteristics were obtained based on the parameters given in the Appendix. The degradation calculation procedure in each iteration step was implanted as presented in Algorithm 1.

Below, we present selected results obtained during the simulation.

Properly developed Algorithm 1 implemented in ABAQUS allowed for the correct prediction of failure of a component subjected to a three-point bending test. In the analyzed element, the failure (scratch due to tension) occurs in the middle of the beam's span. The scratch starts at the top of the notch and moves upwards. The denser grid in the notch area allowed for obtaining a more accurate path for the scratches spreading to the sides and secondary joinings. The three-point bending test is one of the most important tests in crack mechanics. The plastic-degradation model of concrete (Barcelona model) was correctly validated in the Abaqus programme based on experimental research from Piątek-Sierek.[37] Based on these results, we found that the paths visible in the graphs (degradation variable under compression d_c, degradation variable under tension d_t, and stress under strain) from the numerical calculations practically coincide with the experimental studies. The obtained results of the numerical analysis are also in line with the trends presented by Davies.[38]

6 | REINFORCEMENT CONCRETE FORMULATION

6.1 | Constitutive model

In real-life structures, concrete is usually reinforced. It is therefore necessary to account for it in numerical modeling. In this work, we used the Huber–Mises criterion for modeling reinforcement steel.

$$f_s(\boldsymbol{\sigma}, \kappa_s) = q - \sigma_s(\kappa_s), \tag{101}$$

where σ_s the yield strength of steel and κ_s is the reinforcement parameter. The parameter κ_s is identical to linear equivalent deformation as defined by formula (101), assuming $\psi = 0$. This law describes a perfectly elastic–plastic material. This reflects the actual behavior of steel quite well.

In the initial load stage, the steel behaves linearly and elastically until the yield point is reached. Then, the so-called plastic shelf is created and the material gets reinforced. As a result of further loading, the sample is destroyed once it enters the weakening range.

6.2 | Contact between reinforcement and concrete

The Huber–Mises criterion was used to describe reinforcement steel. We abandoned a detailed description of the implementation of this law as it is a special case of the Drucker–Prager criterion, the implementation of which has already been described in Section 3.

The phenomenon of contact between bars and concrete is relatively complicated. Steel is of linear elastic behavior at the initial stage of applying a load, until the yield strength is reached. Afterwards, one can observe the yield plateau and the subsequent material's strengthening. The rupture takes place as a result of the further load application—the sample is damaged after entering the weakening area. The bars' adhesion to concrete depends, among others, on friction on the contact surface, chemical adhesion of steel and concrete, and also concrete shear strength. Thus, the adhesion depends on concrete grade, bars' diameter, their cross-section shape, and the concreting method (concreting direction and compaction in relation to the direction of bars distribution). Two basic damage mechanisms that emerge during extraction of a reinforcement bar from a concrete block can be distinguished. The first one is the so-called splitting damage. It is characterized by cracks parallel to the extracted bar. The second mechanism is the pull-out mechanism, meaning the detachment of a bar from concrete. It appears usually when the traverse compressive stress is introduced apart from the adjacent stresses, which prevents the development of cracks parallel to the bar's axis. It should be noted that there is no universal law describing the contact between steel and concrete. This is due to the fact that laws describing the contact depend on the assumed boundary conditions such as: bar's diameter, concrete grade, side stress, bar's "roughness," and so forth.

When modeling the contact between steel and concrete we employed a solution consisting of defining reinforcement bars as two-dimensional finite elements and declaring two contact surfaces: on the upper and lower edge of the reinforcement. The UINTER procedure was used to implement the slide law. For a given relative displacement δ, it allows for defining the stresses in the direction tangential and normal to the interface edge. For the calculations, we assumed (by assuming a very high "contact stiffness" in a direction perpendicular to the interface axis) that the contact surface cannot open. Adopting high stiffness in the normal direction results in obtaining the same normal displacements for nodes lying on both interface surfaces. The solution described requires the use of a fairly dense FEM grid in the reinforcement neighborhood to avoid deformed elements (too long compared to height).

In Section 6.3, to link the concrete with reinforcement, the shared nodes (SN) method was used. The shared node approach for including reinforcement requires the nodes of the reinforcement grid and concrete mesh to be identical.

In Sections 6.4 and 7, to link the solid element nodes (SOLID) implemented in the plastic-degradation model with the beam element nodes (BEAM) of the reinforcement, the constrained Lagrange in solid (CLIS) node construction method was used. In this method, two FEM grids are superimposed on each other in an appropriate geometrical configuration, and then the internal bond system is constructed to ensure consistent movement of the grids. The required input data include the individual reinforcement and concrete parts, with the reinforcement being considered a slave part, coupled to the concrete master part.

6.3 | Update of the plastic-degradation model including the reinforcement

To use a plastic-degradation model for analysis based on the plastic hinge concept, it must be calibrated with respect to the reinforcement. Such a procedure is a prerequisite for the CDP model to be used in the actual viaduct support. The procedure is intended to check the correctness of the combined concrete and steel parameters assumed for the calculations.

We analyzed a concrete element with size as in Figure 10. The element consists of two parts. The upper part is 1000 mm wide × 10,000 mm high, and the lower part is 4500 mm wide × 10,000 mm high. The analysis was carried out on a 2D model. The shape of the element was modeled on the shape of intermediate support with variable geometry and rigidity, where the upper part is a flaccid element and the lower part is a rigid element.

The model was divided into 54,890 flat 2D four-node ES finite element of CPS4 type and bilateral shape function and 50 mm side. There were 61,657 nodes in total. The calculations were performed for several finite element grid sizes. The greatest convergence was obtained for a grid with a side of 50 mm. The convergence criterion assumed for defining the best mesh discretization was adopted based on displacement at point. The grid size was considered correct when the difference in the displacement results at the point between the two grid pitch sizes was approx. 2%. The load was kinematically modeled in the form of uniform horizontal displacement applied on the very top of the bending element (Figure 10).

For numerical calculations, we used concrete with a compressive strength of $\boldsymbol{f_c} = \mathbf{37\ MPa}$. Reinforcement was made of bars of high ductility steel A-IIIN (BSt500S), with a diameter of φ40, and yield strength of 500 MPa. All necessary material characteristics were obtained based on the parameters given in the Appendix. The degradation calculation procedure in each iteration step was implanted as presented in Algorithm 1.

Below, we present selected results obtained during the simulation.

The results show a clear damage concentration zone exclusively in the area where the concrete is subjected to major tension-related stress. With reinforcement taken into account, this zone dispersed along the reinforcement bars. The

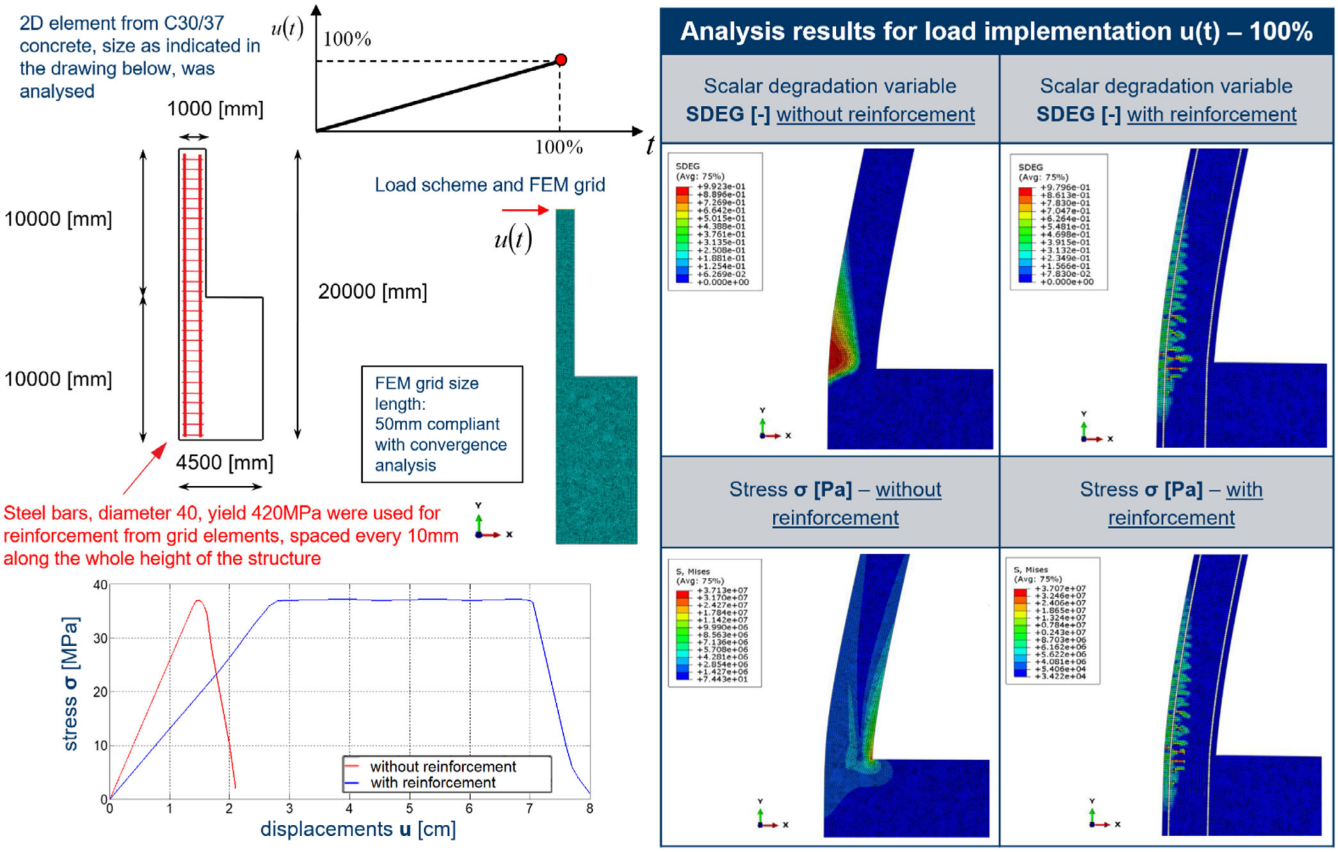

FIGURE 10 Update of CDP model parameters taking reinforcement into account

stress-displacement diagram shows the achieved cross-section plastification. The obtained solution corresponds to the trends found in the literature.

6.4 | Verification of the parameters of the CDP model—Comparison of ABAQUS versus LS-DYNA results

The damage plasticity model required verification prior to its final application. The verification was carried out in the LS-DYNA software, as it is a more effective and efficient tool for studying fast-changing phenomena with the nature of generated waves propagation, for example, an earthquake load. The input data for the verification process were the stress–strain curves σ–ε obtained during the validation and calibration of parameters in the ABAQUS software. The verification procedure consisted of successive iterative simulations aiming at the determination of the magnitude of parameters subjected to the verification, in such a way that the output image (stress–strain curves obtained from the simulation in the LS-DYNA software) was as homothetic as possible to the input image (stress–strain curves obtained from the numerical analyses in the ABAQUS software).

The subject for the verification procedure was the highest support no. 8 of the V17 viaduct, 70 m high (Figure 11). The numerical model of the intermediate support, similarly to the model of the support prepared in ABAQUS, was divided into 65,244 eight-node cubic solid elements of reduced integration with a linear shape function of the C3D8R type, with a total number of nodes equal to 81,345. The basic element dimension of the finite-element grid was $10 \times 100 \times 250\ \mathrm{mm}^3$. The calculations were carried out for several finite-element grid sizes. The greatest convergence was obtained for a grid size of $10 \times 100 \times 250\ \mathrm{mm}^3$. The convergence criterion assumed for defining the best mesh discretization was adopted

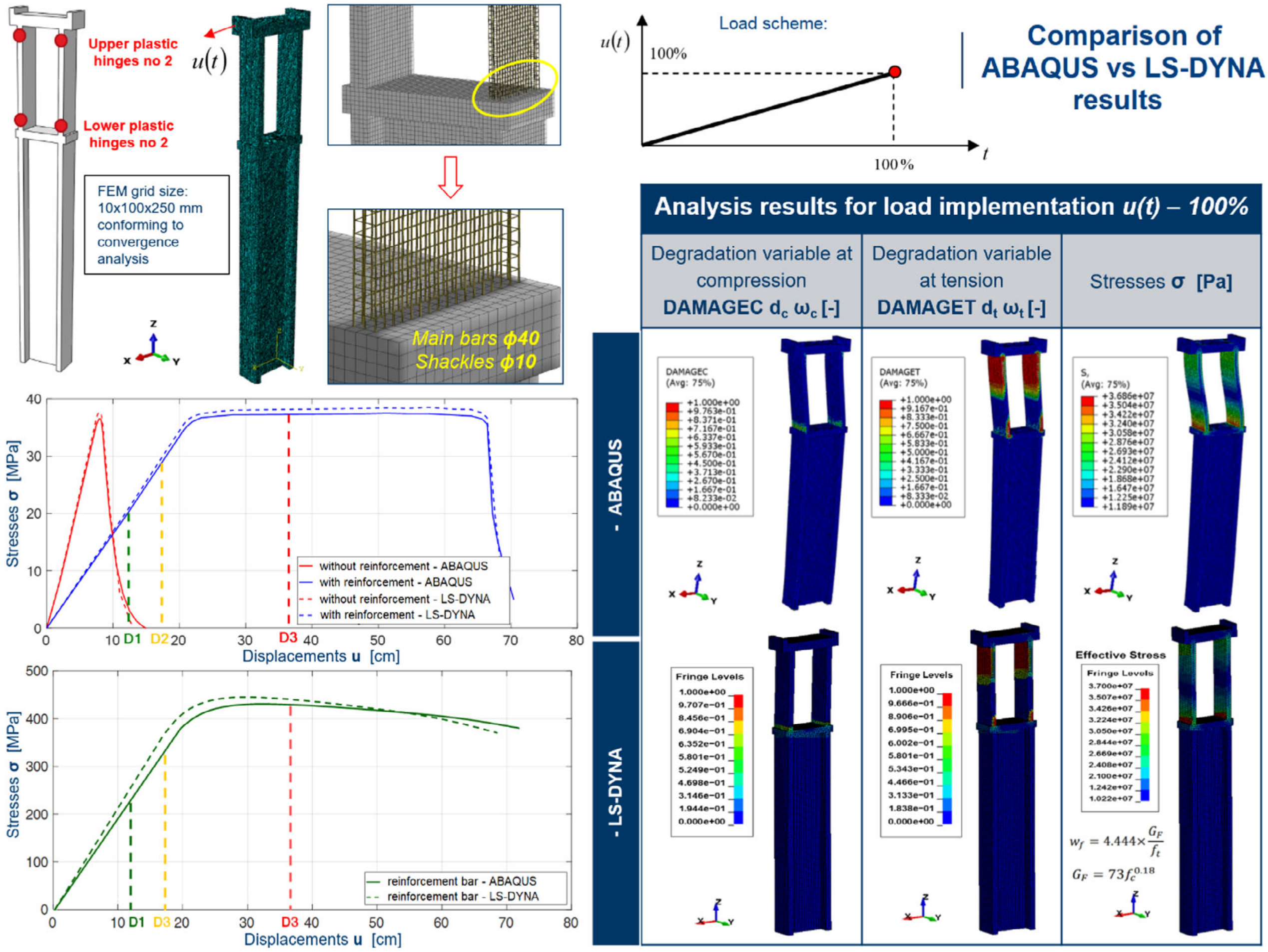

FIGURE 11 Comparison of ABAQUS versus LS-DYNA results

based on displacement at point. The grid size was considered correct when the difference in the displacement results at the point between the two grid pitch sizes was approx. 2%. For the calculations, the parameters of the damage plasticity model of the C 30/37 concrete were used. The reinforcement was constructed of bars with a diameter of 40 mm, made of highly ductile A-IIIN (BSt500S) steel with a yield point of 500 MPa. At the bottom of the support, a fixed joint was executed.

Figure 11 presents a comparison of the results obtained from the numerical analyses performed during the verification in the ABAQUS and LS-DYNA software. The results were read in lower plastic hinges no 2. Based on the obtained results, it was found that the paths in both stress graphs in the translation load domain practically coincide with each other at each time step. The maximum relative error obtained when comparing the stress graphs was approx. 3.12%. It was also shown that the parameters of the compressive degradation variable d_c and the tensile degradation variable d_t, obtained in the LS-DYNA software, were the same as the analogous parameters obtained in the ABAQUS software. The maximum relative error obtained when comparing the parameters was approx. 1.42%. In conclusion, it was found that the verification of parameters of the reinforced CDP model was correct. This allows the CDP model to be used for detailed modeling of the entire V17 viaduct in the LS-DYNA software.

7 | APPLICATION AND SIMULATION

7.1 | Numerical model of the V17 viaduct—Northern Marmara Highway

A correctly calibrated plastic-degradable concrete model (Algorithm 1) with reinforcement has been implemented into the actual structure. A full and detailed 3D model of the V17 viaduct, which is part of the Northern Marmara Highway in Istanbul, was subjected to parametric tests. The main objective was to carry out a detailed analysis of the dynamic response including material degradation in the LS-DYNA programme (Figure 12), similar to Miśkiewicz et al.[39] A super-fast, high-power computer called TRITON, available at the Gdansk University of Technology (it is one of the 100 fastest computers in the world) was used for the calculations. All the supports in the model were made according to the new concept of shaping supports with variable geometry and rigidity. The platform has a box cross-section. Dilatation was made in a platform divided into 13 segments. Parameters of the plastic-degradation model of CDP concrete with C 30/37 strength according to Annex 1 were used for calculations. Bars of diameter φ40 made of steel with a yield strength of 420 MPa were used for the main reinforcement of the intermediate supports. Shackles were made from φ10 bars. We drafted a full tensioning of the viaduct platform. The degradation calculation procedure in each iteration step was implanted as presented in Algorithm 1.

The V17 model was divided into 565,244 8 node cubic solid elements of reduced integration with linear shape function type C3D8R, with the total number of nodes being 681,345. The basic dimension of the ES finite element grid is $250 \times 250 \times 250\ \text{mm}^3$. The calculations were performed for several finite element grid sizes. The greatest convergence was obtained for a grid sized $250 \times 250 \times 250\ \text{mm}^3$. The convergence criterion assumed for defining the best mesh discretization was adopted based on displacement at point. The grid size was considered correct when the difference in the displacement results at the point between the two grid pitch sizes was approx. 2%.

A restrain was made at the bottom of all supports. The platform was supported on intermediate supports by the intermediary of elastomeric bearings reducing vibrations transferred from the support to the platform.

7.2 | Elastomer bearing model

To prepare the numerical model of the elastomer bearing, the SLEB model (available in the code of the LS-DYNA programme) was used. SLEB consists of rubber and steel, in which a hyper-viscoelastic model was used to correctly map the strain of the rubber. As for the steel washers, it was presumed that the strain values in all directions were small. For the steel washers, the material elastic model was used during the FEM analysis.

The rubber material used in the elastomeric bearings supporting the platform on the supports requires hysteretic behavior. Since its role is to reduce the inertial forces of the bridge and absorb the earthquake energy. At the macroscopic level, rubber can undergo large elastic strains; it also changes its volume to a very small extent and in terms of the dimensions when pressure is applied. The main reason for these features is that the strain of rubber is closely related to the strengthening of the molecular chains. When it comes to the elastomers, they are almost incompressible. Therefore,

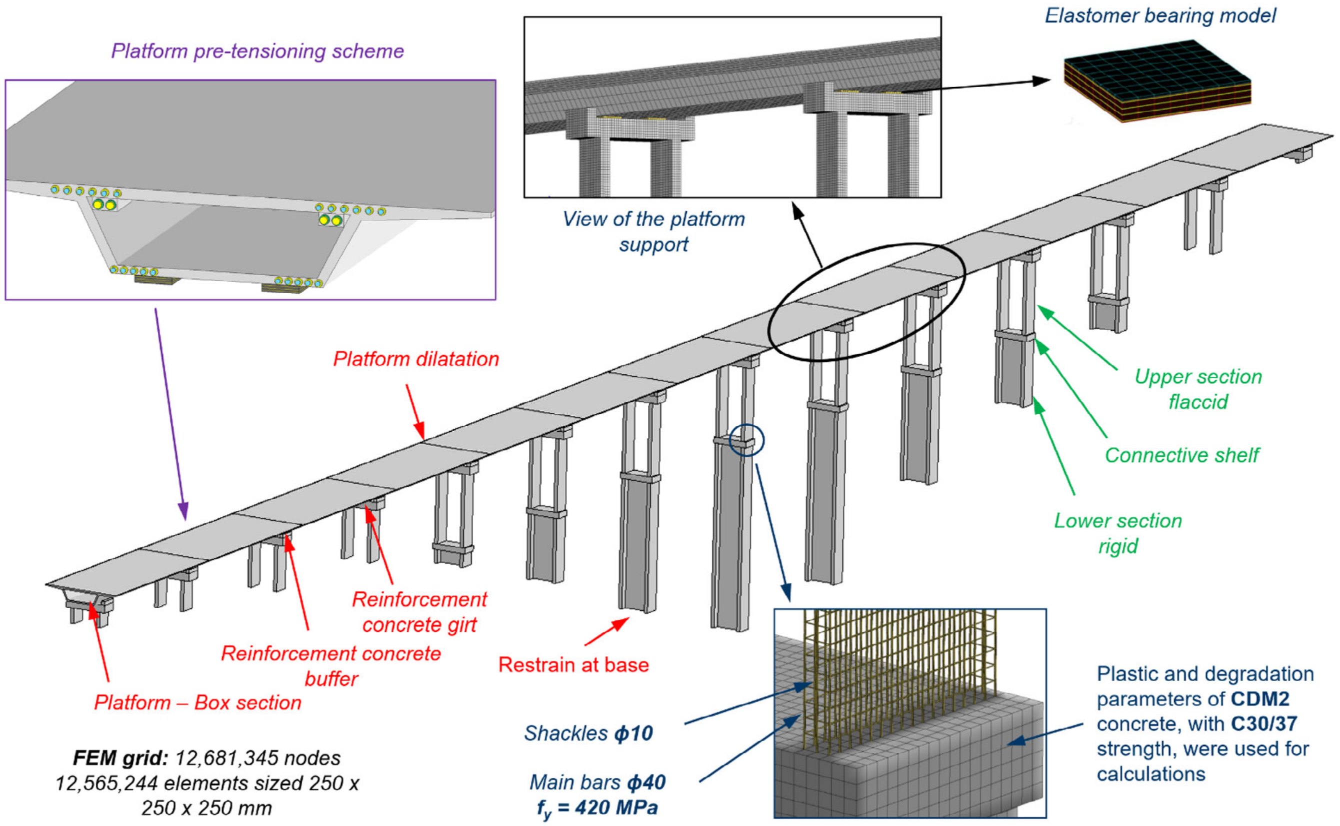

FIGURE 12 Numerical 3D model of the V17 viaduct with details in LS-DYNA

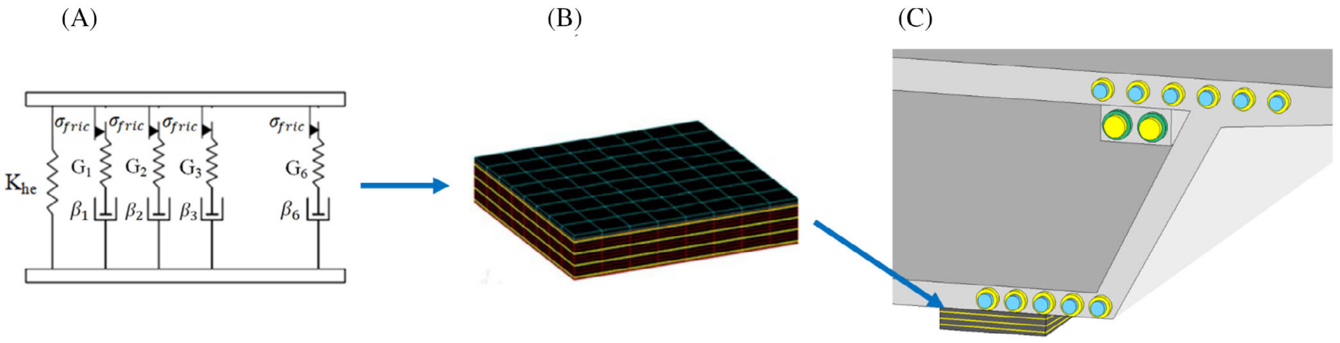

FIGURE 13 (A) Mechanical representation of the hyperviscoelastic, (B) numerical model of the elastomer bearing in LS-DYNA, (C) supporting the platform on an elastomer bearing in LS-DYNA

precise modeling of damping rubber bearings requires the creation of a joint with low compressibility, kinematic nonlinearity and nonlinearity of the material. When analyzing scientific literature, several models were found for components made of rubber.[40–44] Salomón et al.[44] in their research paper proposed a constitutive model of rubber with the use of high damping. In this model, the behavior of the hysteretic rubber component is initiated using viscoelastic and plastic constitutive models. On the other hand, Yoshida et al.[43,45] modeled the constitutive relationships of rubber by combining a hyperelastic damage model with elastoplasticity, which works according to the hardening law being dependent on the isotropic strain.

To the rubber model, a hyper-viscoelastic model was applied consisting of a hyperelastic model connected parallelly with the Maxwell viscoelastic model, similar to Ambrosio et al.[40] Figure 13 shows the mechanical representation of this model. In this model, the K_{he} spring reflects the hyperelastic part. By contrast, six modified Maxwell models reflect the viscous part of the rubber material. An explanation of the mathematical forms of these two main parts of the hyper-viscoelastic constitutive model is presented below.

When it comes to the hyperelastic part, the strain energy density function W of the Ogden's polynomial[46] amounts to:

$$W\left(J_1, J_2, J\right) = \sum_{p,q=0}^{n} C_{pq}(J_1 - 3)^p (J_2 - 3)^q + W_H(J) \tag{102}$$

with

$$J_1 = I_1 J^{-\frac{1}{3}},\ \ J_2 = I_2 J^{-\frac{1}{3}},\ \ J = \lambda_1 \lambda_2 \lambda_3 = \frac{V}{V_0}. \tag{103}$$

In the formula above I_1, I_2, and I_3 are the first, second, or third invariant of strain, respectively. Whereas J_1 and J_2 are the deviator invariants related to them. J is calculated according to the formula (103) and represents the volumetric ratio, where V_0 and V are the original and final volume values, respectively. The coefficients λ_1, λ_2, and λ_3 are the main tension coefficients and p and q represent the polynomial's degree for $J_1 - 1$ and $J_2 - 1$, respectively. In Equation (102), the $W_H(J)$ parameter is the volumetric parameter of the strain energy functional. The $W_H(J)$ parameter is a function of the volumetric ratio of J. When analyzing Equation (52), it can be noted that it is possible to calculate the C_{pq} value by starting with determining the stress–strain relationships assuming the values of 0, 1, 2, or 3 for n in the code ascribed to the material in the LS-DYNA programme.

The polynomial form for tensile strains for $n = 2$ may be valid up to 90%–100%. It is appropriate to bear in mind that the values can cause the emergence of inflection points on the stress–strain curve. On the other hand, for deformations ranging from 100% to 200%, five-term and nine-term polynomials can be used.

In order to consider the hysteretic behavior of the rubber element, the modified Maxwell model was adopted during calculations, taking into account the friction damping, as shown in Figure 13. When applying simple viscoelastic relations, the relaxation function of the viscoelastic theory is modeled with the aid of a six-segment Prony's series:

$$g(t) = \sum_{i=1}^{6} G_i e^{-\beta_i t}, \tag{104}$$

where G_i is the shear relaxation modulus for the ith part. The β_i parameter is a damping constant dependant on time t. Using Equation (104), 12 values (G_i, β_i, $i = [1\ \ldots\ 6]$) have to be included. In the LS-DYNA programme,[47,48] G_i for $i = 1{\sim}6$ is set as a constant value. During the numerical analysis, the limit stress (SIGF) σ_{fric} was assumed for the friction damping which is frequency-independent. As well, default values of damping constants were assumed for five β_i ($i = 3, 3{\sim}6$). In compliance with the user manual of the LS-DYNA programme, a value of zero was assigned for the parameter β_1, while β_3 is the decuple value of β_2, and β_4 is a hundred times greater than β_3, and so on.

During the modeling: the values of the limit stress σ_{fric}, shear modulus G and modified Maxwell model as well as the damping constant β_2 (BSTART in LS-DYNA) were achieved by adjusting the hysteretic loop area in response to loading and unloading.

MAT_77H_HIPERVISCOELASTIC_RUBBER was entered into the program in an input file, which included a graph of the stress–strain-deformation relationship for rubber, yield strength σ_{fric}, shear modulus G_i, density, Poisson's coefficient, dynamic viscosity coefficient n, and friction coefficient. The steel spacer was modeled using MAT_ELASTIC because its deformation values are relatively small. MAT_ELASTIC has been entered into the program in an input file specifying the density, Young's modulus, Poisson's coefficient. The contact between the rubber part and the steel spacers was made as a frictional-anti-slip contact.

Property parameters of the material accepted for analysis: mass density 10^3 kg/m^3, shear modulus independent of shear frequency $G = 19.4635$ MPa, stress limit SIGF $= 0.3$ MPa, Poisson's coefficient $\nu = 0.49$, decay constant (BSTART) $= 0.0001$, rise time $= 0$. To analyze the deformation of steel spacers, the MAT_ELASTIC material model was used with the following properties: Young's modulus $E = 200$ GPa and Poisson's coefficient $\nu = 0.29$. The contact between the rubber part and the steel spacers was made as a frictional-anti-slip contact.

7.3 | Platform prestressing model

The V17 viaduct platform is a prestressed structure (Figure 14), into which the internal forces opposing the loads acting on the structure were deliberately introduced. The platform's load-bearing structure is prestressed by

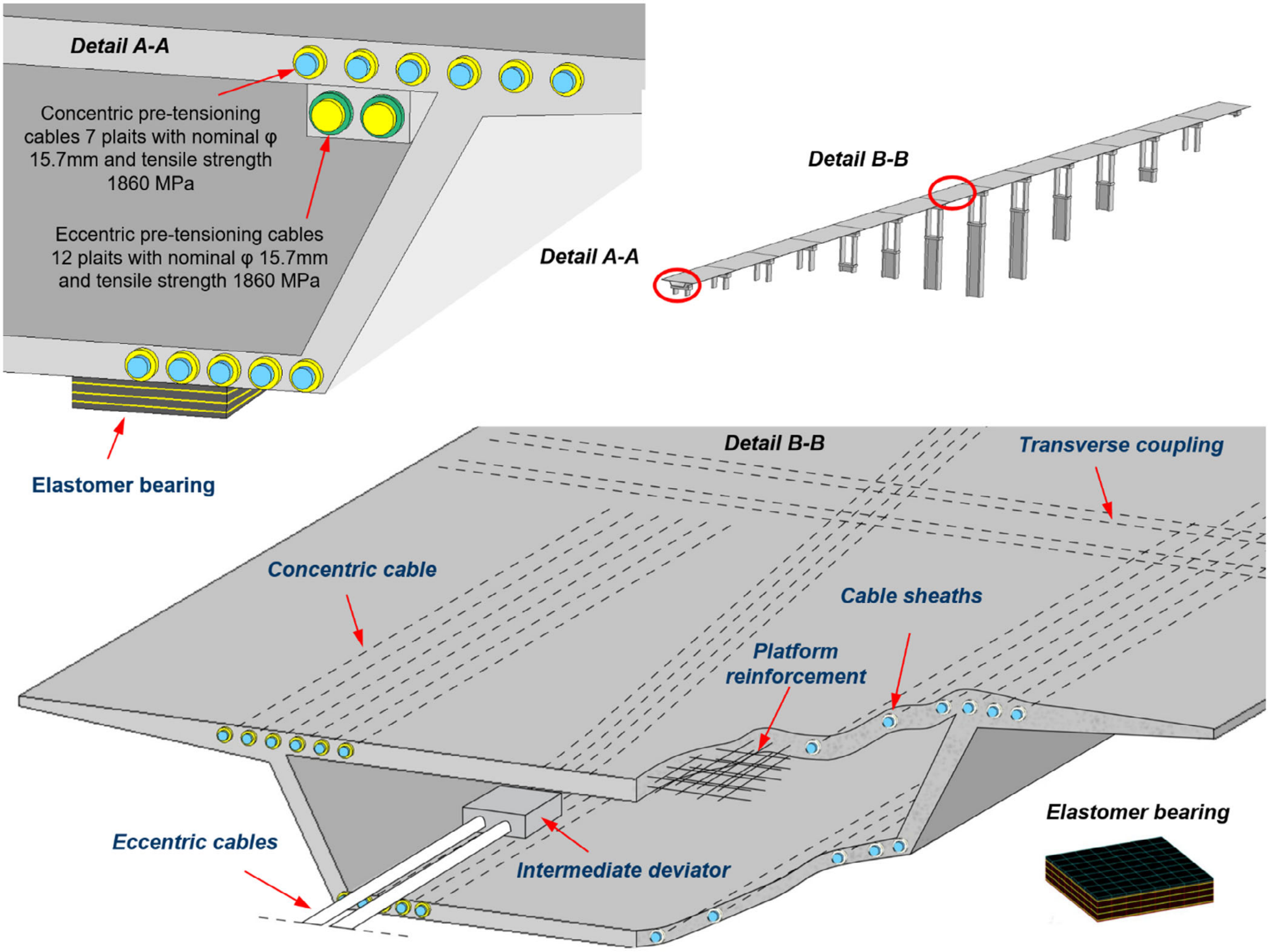

FIGURE 14 Numerical prestressing model for V17 viaduct platform in LS-DYNA

centric compression cables, located in both the top and bottom plates, and eccentric cables. The eccentric prestressing cables run through the length of two spans and are anchored passing on the deviators located in the top plate.

The cables are deflected by intermediate deviators located in the bottom plate. The inner tension members are tensioned after the concrete mix has cured. Special protective tubes ("ducts") were used to prevent contact between the cable and the concrete mix. A group of tension members in one sheath is called a cable. The cables were stretched once the concrete has reached the appropriate compressive strength. Freyssinet C system cables were used for internal prestressing. The external prestressing was carried out with external cables consisting of 7, 9, and 12 strands with a nominal diameter of 15.7 mm and a nominal tensile strength of 1860 MPa. In addition, reinforcement made of bars with diameter φ40 of high ductility steel A-IIIN (BSt500S) with yield strength of 420 MPa were modeled in the platform.

The desired type of prestressing in the FE-model was a post-tensioning, which was then grouted before any external load was applied. To achieve this effect the modeling was divided into four steps, each representing a step taken in real life when applying prestressing to a post-tensioned beam.

7.3.1 | Stage I—Creating the prestressing duct

At the very beginning, a numerical model of the prestressing ducts was developed by placing "guiding cables" along the predetermined position of the prestressing ducts. The numerical model of the guiding cables was executed using beam elements to which the *MATNULL material was ascribed. The application of *MATNULL means that the prestressing ducts will not have any impact on the rigidity of the structure. To connect the prestressing ducts to the surrounding concrete, *CONSTRAINED-LAGRANGE-IN-SOLID was used. Reinforcement was supplied by a joint with the concrete using the same method (Figure 14).

7.3.2 | Stage II—Placing of the prestressing wires into the ducts

In the second stage, a model for prestressing strands was designed with use of beam elements. The beam elements used were placed along the same line and featured the same geometry as the guiding cables. The same type of *MAT-PLASTIC-KINEMATIC material as used for the reinforcement was ascribed to the prestressing strands. Then, the prestressing strands were placed inside the prestressing ducts by implementing a *CONTACT-GUIDED-CABLE-SET set of contacts between the prestressing ducts and the prestressing strands. The contact made allows the strands to slide freely inside the ducts and also causes the prestressing strands to exert pressure on the circumjacent concrete when the parabolic strands are tensioned. The modeling method for Stage 2 is shown in Figure 14. In order to obtain free movement of the prestressing strands inside the ducts, an identifier of the set of parts consisting of beam elements representing the prestressing strands as well as an identifier of the node set—that is, beam element nodes representing the guiding cables—were defined in the contact card. Thanks to this approach, beam elements of the prestressing strands were able to move between the nodes of beam elements of the guiding cables.

7.3.3 | Stage III—Tensioning the platform segments

The platform segments were tensioned on both sides. At the ends of the platform segments, anchor plates were modeled by implementing nodal sets of rigid bodies—that is, nodes that together formed inelastic surfaces. With the aim of obtaining the tensioning effect, the material of the external beam elements of the prestressing strand was changed to *MAT-ELASTIC–PLASTIC-THERMAL. This material features thermoelastic properties, thanks to which it may deform under the impact of thermal gradients. The nodes of those thermal beam elements are pasted together on one side with one of the nodes of the anchoring plate and pasted together on the other side with the prestressing wire. The guiding cable must not be pasted to the tensioning element.

After completing the entire model of the prestressing mechanism for the individual segments of the platform, the negative temperature load on the nodes of the tensioning elements was defined. Its purpose was to give them a negative strain. This operation was performed using the 'Thermal Variable' function of the LS-DYNA programme. Since the tensioning elements were pasted to the anchoring plates as well as to the prestressing wire, it starts to pull within them, introducing a normal force to the bridge deck.

7.3.4 | Stage IV—Grouting of the prestressing ducts the platform sections

In the last stage, post-tensioned structures are grouted soon after the tensioning phase. As a result, full compatibility of the strain between the tensioning steel and the circumjacent concrete was achieved. In the FE model, the grouting was modeled by defining the *CONSTRAINED-LAGRANGE-IN-SOLID contact between the prestressing steel and the circumjacent concrete. Only after the tensioning of the individual platform segments was complete was full contact activated. The contact activation delay was possible and controlled using the 'Birth' option in the Lagrange contact card.

7.4 | Plastification of reinforcement section based on the DDC method

The seismic design of the V17 viaduct supports for the Northern Marmara Highway ring road was based on the DDC method, also known as the ductility assumption. The concept consists of determining plastic hinges with a limited degree of computational movement capacity in selected sections of supports. The ductility of the plastic hinges is the strength criterion. The calculations are made to check the demand for ductility based on external loads. The dimensioning is based on the internal forces obtained from the plastification of the hinge design length.

All columns in soft or liquefiable soils, pier walls, and pile/pile-extensions in slab bridges (designed and detailed to behave in a ductile manner) are designated as seismic-critical members. A ductile member is defined as any member that is intentionally designed to deform inelastically for several cycles without significant degradation of strength or stiffness under the demands generated by the design seismic hazards.

Seismic-critical members may sustain damage during a seismic event without leading to structural collapse or loss of structural integrity. Other bridge members such as dropped bent cap beams, outrigger bent cap beams, and abutment diaphragm walls shall be designed and designated as seismic-critical if they will experience any seismic damage. All other components not designated as seismic-critical shall be designed to remain elastic in a seismic event.

Local member displacement capacity, $\boldsymbol{\Delta_c}$ is defined as a member's displacement capacity attributed to its elastic and plastic flexibility. The structural system's displacement capacity, $\boldsymbol{\Delta_c}$ is the reliable lateral capacity of the bridge or subsystem as it approaches its collapse limit state. Ductile members must meet the local displacement capacity requirements and the global displacement criteria.

The local displacement capacity of a member is based on its rotation capacity, which in turn is based on its curvature capacity. The curvature capacity shall be determined by $\boldsymbol{M - \phi}$ analysis. The local displacement capacity, $\boldsymbol{\Delta_c}$ of any column may be idealized as one or two cantilever segments (Figure 15), where

$$\boldsymbol{\Delta_{c1} = \Delta_{Y1}^{\mathrm{col}} + \Delta_{p1}, \quad \Delta_{c2} = \Delta_{Y2}^{\mathrm{col}} + \Delta_{p2},} \tag{105}$$

$$\boldsymbol{\Delta_{Y1}^{\mathrm{col}} = \frac{L_1^2}{3}\phi_{Y1}, \quad \Delta_{Y2}^{\mathrm{col}} = \frac{L_2^2}{3}\phi_{Y2},} \tag{106}$$

$$\boldsymbol{\Delta_{p1} = \theta_{p1}\left(L_1 - \frac{L_{p1}}{2}\right), \quad \Delta_{p2} = \theta_{p2}\left(L_2 - \frac{L_{p2}}{2}\right),} \tag{107}$$

$$\boldsymbol{\theta_{p1} = L_{p1}\phi_{p1}, \quad \theta_{p2} = L_{p2}\phi_{p2},} \tag{108}$$

$$\boldsymbol{\phi_{p1} = \phi_{u1} - \phi_{Y1}, \quad \phi_{p2} = \phi_{u2} - \phi_{Y2}.} \tag{109}$$

The local ductile capacity of an element is the ratio of total displacement to displacement in the elastic state during rotation of the plastic hinge and is expressed in formulas:

$$\boldsymbol{\mu_{c1} = \frac{\Delta_{c1}}{\Delta_{Y1}^{\mathrm{col}}}, \quad \mu_{c2} = \frac{\Delta_{c2}}{\Delta_{Y2}^{\mathrm{col}}}.} \tag{110}$$

Each component should have a minimum ductile capacity equal to $\mu_{c1} \geq 3$ and $\mu_{c2} \geq 3$ to ensure reliable rotation capacity at the point where the plastic hinge is formed, see Caltrans[49] and Kazantzi.[50]

The plastic moment capacity of all ductile concrete members shall be calculated by $M - \phi$ analysis based on expected material properties. Moment curvature analysis derives the curvatures associated with a range of moments for a cross-section based on the principles of strain compatibility and equilibrium of forces. The $M - \phi$ curve can be idealized with an elastic perfectly plastic response to estimate the plastic moment capacity of a member's cross-section. The elastic portion of the idealized curve should pass through the point marking the first reinforcing bar yield. The idealized plastic moment capacity is obtained by balancing the areas between the actual and the idealized $M - \phi$ curves beyond the first reinforcing bar yield point.

During the analysis, the equations of motion integration were initiated by an explicit method in the multi-step type a version (acceleration). The motion equation discretized within FEM at time n was expressed as:

$$M\ddot{x}^n = r^n - f^n - h^n. \tag{111}$$

In this equation, M is the global mass matrix of the system, r^n is the nodal vector of external forces, f^n is the nodal vector of forces accumulating internal impacts and dampings, h^n is the nodal vector resulting from the hourglass control, and $\ddot{x}$ is the vector of nodal accelerations.

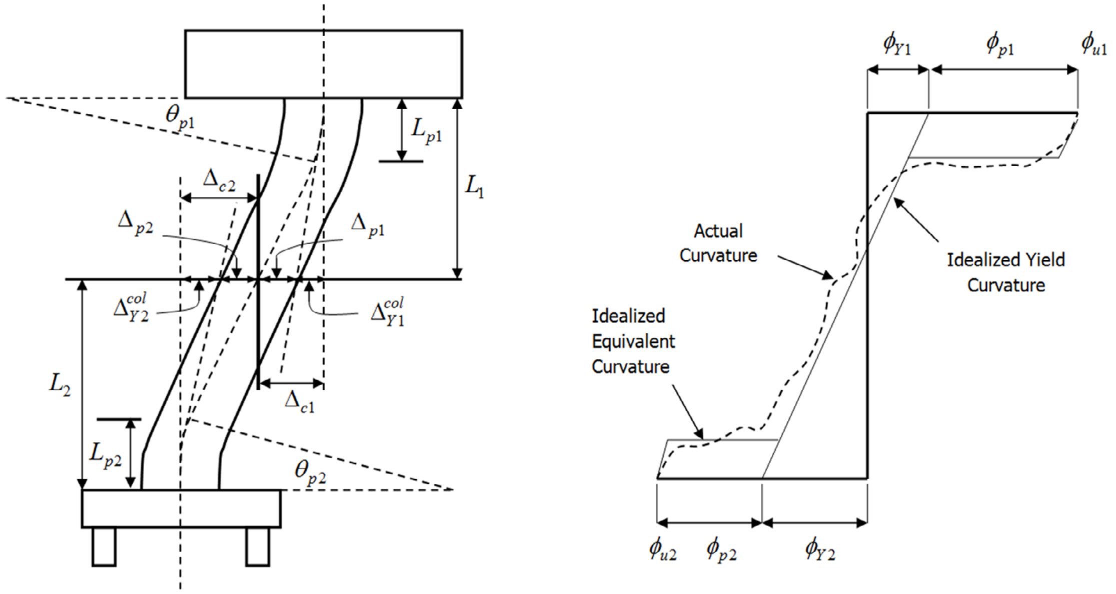

FIGURE 15 Local displacement capacity—Framed column, assumed as fixed–fixed

The applied explicit method is conditionally stable. In order to ensure the solution's stability, the integration step size cannot exceed a certain critical value related to time necessary for the sound wave to pass through a finite element. The time step was determined from the following formula:

$$\Delta t = \alpha \Delta t_{\mathrm{crt}} \leq \min \frac{l_e}{c_e}. \tag{112}$$

In the above equation, α is the Courant number, l_e is a characteristic length of a finite element, c_e is the velocity of sound wave in a material.

The results of numerical simulations of the V17 viaduct showing plastification of intermediate supports based on the DDC method are presented below. The viaduct structure was loaded with acceleration from the Kocaeli earthquake's most intense D3 level according to the Turkish DLH 2008 standard[51] (Figure 16).

Based on the results obtained, we found that the plastic hinges will be formed only in the upper and lower part of the flaccid support. In the order from the highest to the lowest support. The platform broke in two places (Figure 16).

The lower plastic hinge was formed at a height of 80 cm (Figure 17). An upper plastic hinge was formed at the same height because the distribution of bending moments at the top and the bottom of the flaccid support are identical (Figure 18). The reinforcement bars have reached the yield point of 433 MPa.

In summary of the results obtained, we have shown that the DDC method does not take into account the actual method of joining the individual reinforcement parts in the transition zone, between independently concreted elements. This results in a dynamic analysis over-generalization of the structure and consequently incorrect results. The DDC method for determining the plastic hinges in intermediate supports is far from perfect because it does not reflect the reinforcement's transition zone between the rigid part and the flaccid support.

8 | NEW DDC2 PLASTICITY DETERMINATION ALGORITHM

As the DDC method proved to be imperfect, a new algorithm for determining cross-section plastification parameters called DDC2 was developed. The new algorithm consists of two parts. The first part describes how the concrete is degraded, while the second part describes the plastification of the reinforcement bars taking into account the reinforcement bond's transition zone.

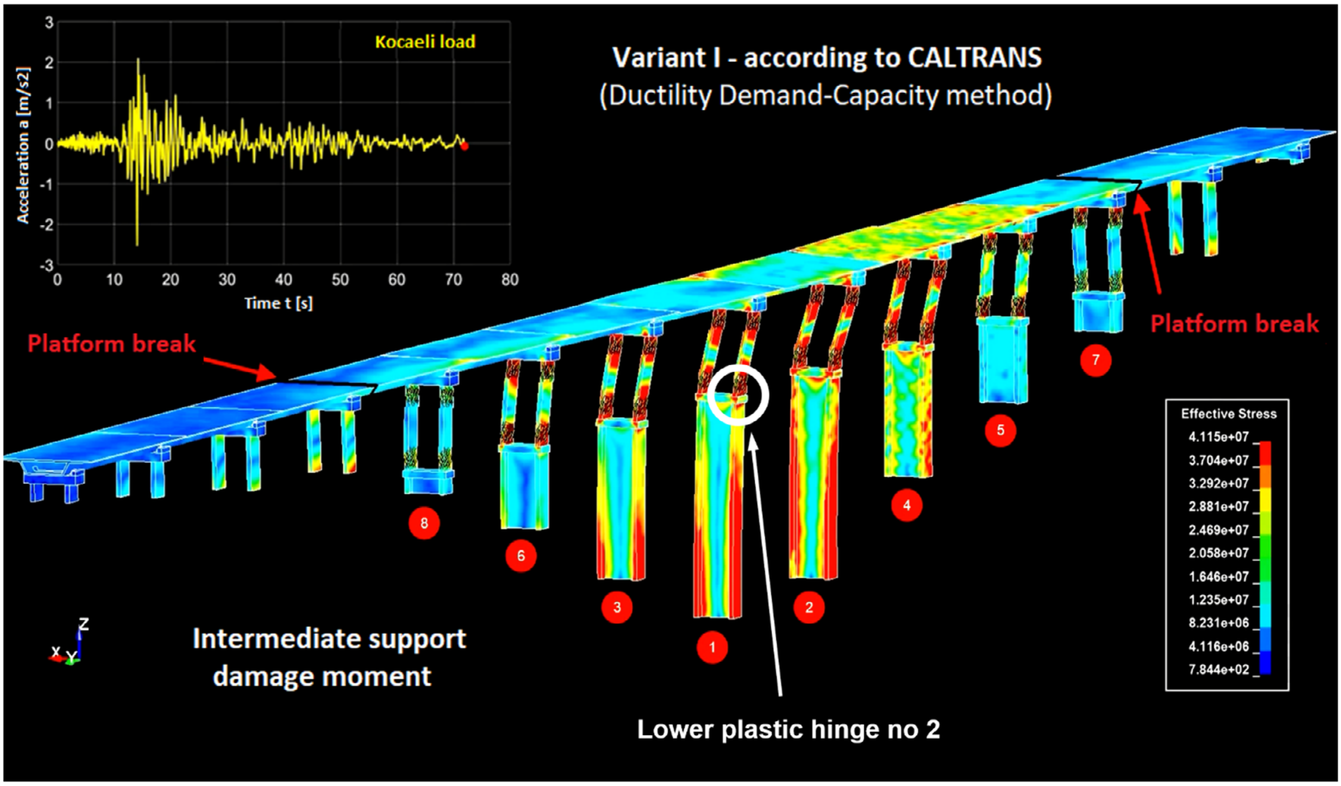

FIGURE 16 The results of numerical simulations of the V17 viaduct of intermediate supports based on the Ductility Demand-Capacity method

---

Algorithm 2. New algorithm DDC2 for determining cross-section's plastification parameters

---

PART 1: *Concrete degradation*

1. Determination of the elastic stiffness matrix $\boldsymbol{C}^e$

2. Deformations at the beginning of the increment $(\varepsilon)^{t+\Delta t} = (\varepsilon)^t + \Delta\varepsilon$

3. Effective deformation $(\tilde{\varepsilon})^{t+\Delta t} = \exp\left(-L^2/2\right)(\varepsilon)^{t+\Delta t}$

4. Effective stresses $\tilde{\boldsymbol{\sigma}} = \boldsymbol{C}^e : (\tilde{\varepsilon})^{t+\Delta t}$

5. Determination of the non-local elastic deformation energy $\overline{Y}^*$ from Equation (48)

6. Checking for plastification $f\left(\overline{Y}^*\right) - r\left(L^{t+\Delta t}\right) \geq 0$

7. If condition (6) is met:

a) initialization: $f^{(0)} = f\left(\overline{Y}^*\right), \quad \Delta L^{(0)} = 0, \quad i = 0$

b) calculating correction δL (wzór 22) and updating of the increment $\Delta L^{(i+1)}$ calculating correction $\delta\lambda$ (wzór 10) and updating $\Delta\kappa^{(i+1)}$ calculation of the non-local reinforcement parameter $\left(\Delta\hat{\kappa}^*\right)^{(i+1)}$ (Equation 46)

c) update of the load function $f\left(\overline{Y}^*\right)^{(i+1)}$

d) verification of the convergence condition $\left|f\left(\overline{Y}^*\right)^{(i+1)} - r\left(L^t + \Delta L^{(i+1)}\right)\right| \leq Tr^{(0)}$

8. If condition (7d) is met: stress update $\boldsymbol{\sigma}^{t+\Delta t}$ (Equation 26) or determination of strains $(\varepsilon^e)^{t+\Delta t}$ and $(\varepsilon^p)^{t+\Delta t}$ (Equations 20 and 21), otherwise, return to point (7b)

9. If condition (6) is not met: $L^{t+\Delta t} = L^t$

10. Implementation of: elastic–plastic model's parameters with stiffness degradation that characterize the plastic deformations emergence, variable compressive and tensile deformation, and the parameters that can simulate the *stiffness recovery effect*—according to the Appendix

PART 2: *Reinforcement bar plastification with reinforcement transition zone taken into account*

1. Calculating idealized yield curvature defined by an elastic-perfectly-plastic representation of the cross ϕ_{Yi}

2. Calculating distance from the point of maximum moment to the point of contra-flexure L_i

3. Determining the idealized yield displacement of the column at the formation of the plastic hinge $\Delta_{Yi}^{\mathrm{col}} = \frac{L_i^2}{3}\phi_{Yi}$ (Equation 56)

4. Determination of the transition zone range $L_{p2}^{\mathrm{zone}} = \max(0.3L_i; 1.5\ \mathrm{m})$

5. Calculating equivalent analytical upper plastic hinge length $L_{p1} = \begin{cases} 0.08L + 0.15f_{ye}d_{bl} \geq 0.3f_{ye}d_{bl} \\ 0.08L + 0.02f_{ye}d_{bl} \geq 0.4f_{ye}d_{bl} \end{cases}$

6. Calculating equivalent analytical lower plastic hinge length $L_{p2} = \begin{cases} 0.08L + L_{p2}^{zone} + 0.15f_{ye}2d_{bl} \geq 0.3f_{ye}d_{bl} \\ 0.08L + L_{p2}^{zone} + 0.02f_{ye}2d_{bl} \geq 0.4f_{ye}d_{bl} \end{cases}$

7. Determining curvature capacity at the failure limit state, defined as the concrete strain reaching or the longitudinal reinforcing steel reaching the reduced ultimate strain φ_{ui}

8. Calculating idealized plastic curvature capacity (assumed constant over L_{pi}) $\varphi_{pi} = \varphi_{ui} - \varphi_{Yi}$ (Equation 59)

9. Calculating plastic rotation capacity (radian) $\theta_{pi} = L_{pi}\varphi_{pi}$ (Equation 58)

10. Determining idealized plastic displacement capacity due to rotation of the plastic hinge $\Delta_{pi} = \theta_{pi}\left(L_i - \frac{L_{pi}}{2}\right)$ (Equation 57)

11. Determination of total elastic and plastic displacement $\Delta_{ci} = \Delta_{Yi}^{\mathrm{col}} + \Delta_{pi}$ (Equation 55)

Calculations according to the new DDC2 algorithm have been made for two reinforcement shape variants in the transition zone (i.e., at the point of joining the flaccid part of the support with the rigid part, Figure 19). According to the V17 viaduct design and the solutions commonly used in the construction industry, the first variant assumed making a reinforcement bond transition zone between the rigid part and the flaccid part of the support at the starters heights equal 150 cm $\left(L_{p2}^{\mathrm{zone}} = \max(0.3L_i; 1.5\ \mathrm{m})\right)$. In line with our solution, the second variant assumes the construction of the reinforcement joint transition zone at the height of min. 315 cm $\left(L_{p2}^{\mathrm{zone}} = \max(0.3L_i 1.5\ \mathrm{meters}), \text{where } L_i = 10.5\ \mathrm{m}\right)$.

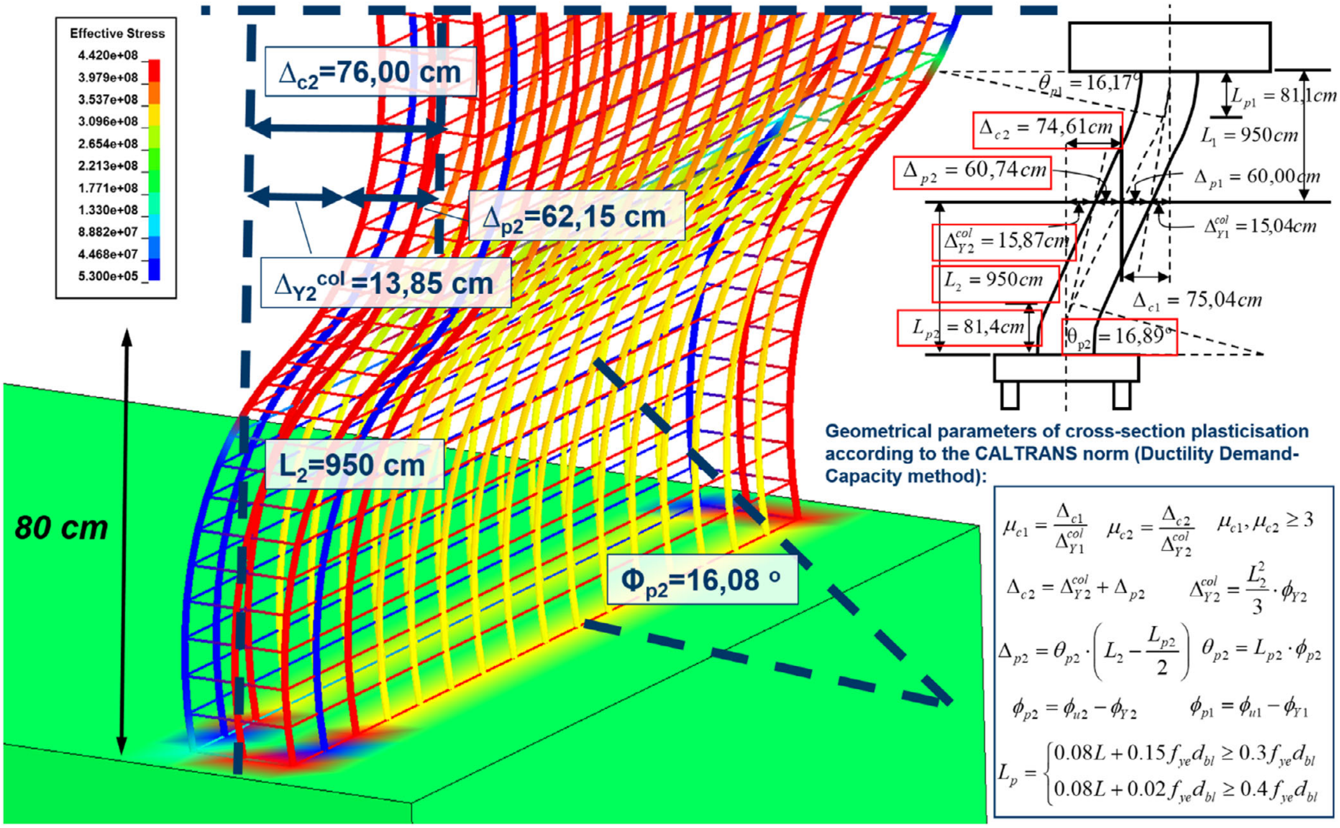

FIGURE 17 Local displacement capacity - lower hinge

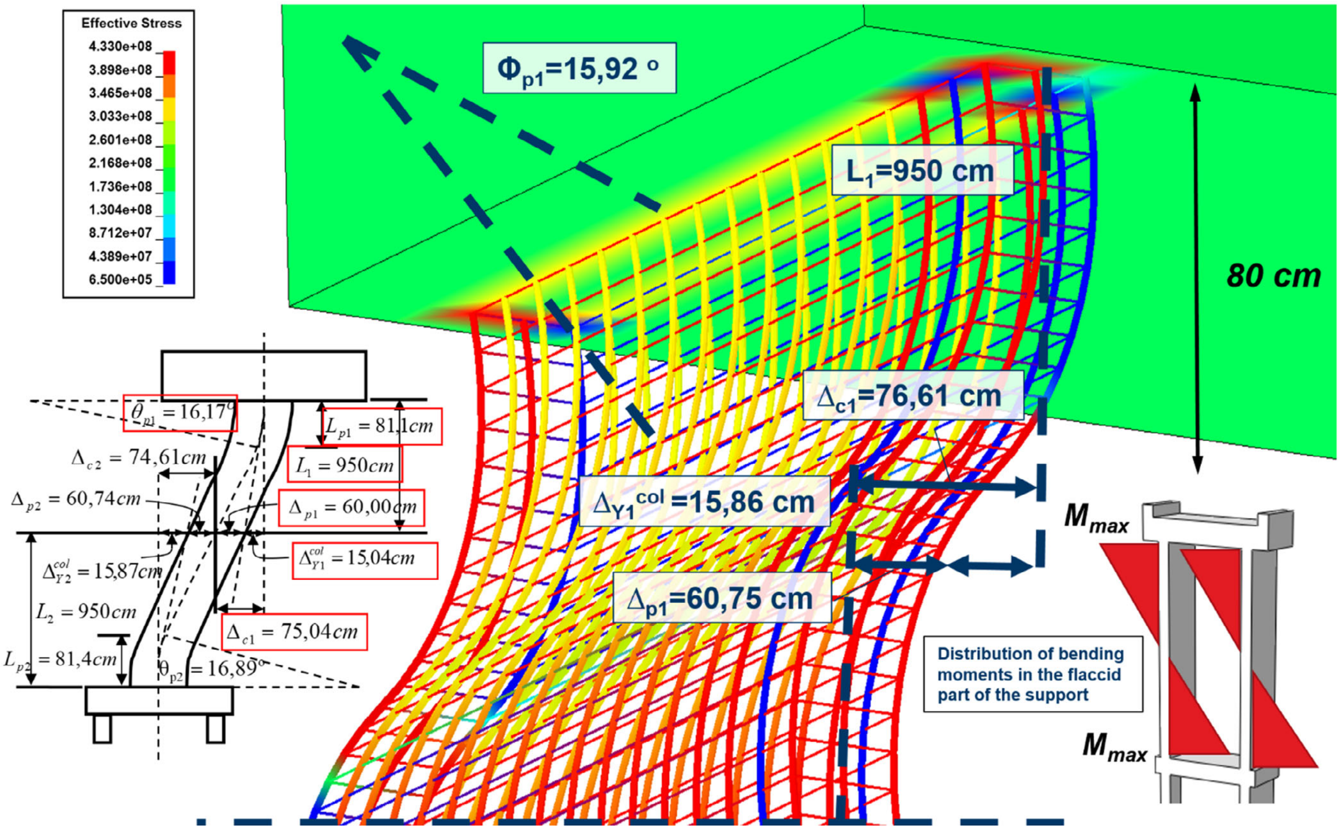

FIGURE 18 Local displacement capacity - upper hinge

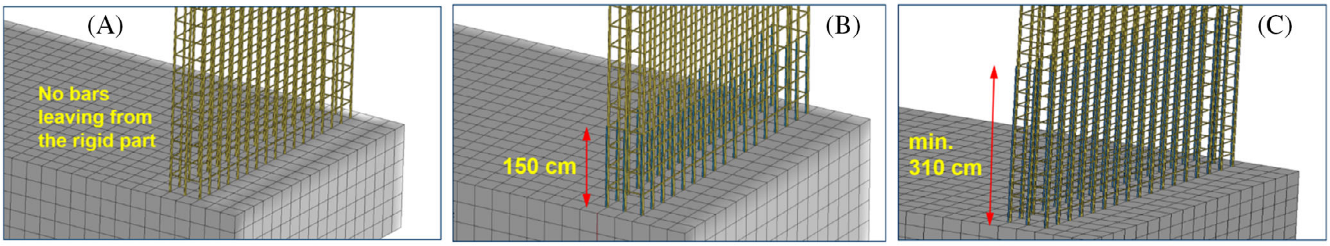

FIGURE 19 Comparison of the transition zone shape according to: (A) DDC method (Algorithm 1), (B) variant I, and (C) variant II—DDC2 method (Algorithm 2)

During the modeling of the connection of bars in the transition zone, boundary conditions were created describing the connection of bars coming from the rigid part with bars located in the flaccid part of the support. The CONSTRAINED_GENERALIZED_WELD_SPOT function was used to describe this connection. The nodes of the bars (rigid part and flaccid part) are spot welded together with failure criteria.

The first variant subjected to numerical calculation, based on the new DDC2 algorithm to determine the section plasticity, was variant I of the reinforcement formation in the transition zone of the intermediate support. The results obtained during the numerical analysis are presented below (Figures 20 and 21).

Figure 20 shows the state of degradation of the supports just before they were completely destroyed after the application of the FEM grid. Their condition is shown for the highest support nos. 7, 8, and 9. As a result of high vibrations, the platform destroyed a reinforced concrete buffer designed to absorb vibrations.

Figure 21 shows the destruction of the V17 viaduct after the Kocaeli level D3 earthquake. The platform pre-tensioning cables were broken. Then, the platform's reinforcement and elastomer bearings got completely destroyed. The bearings got worn off and the stresses reached their limit value. The obtained results showed that the lower plastic hinge appears at

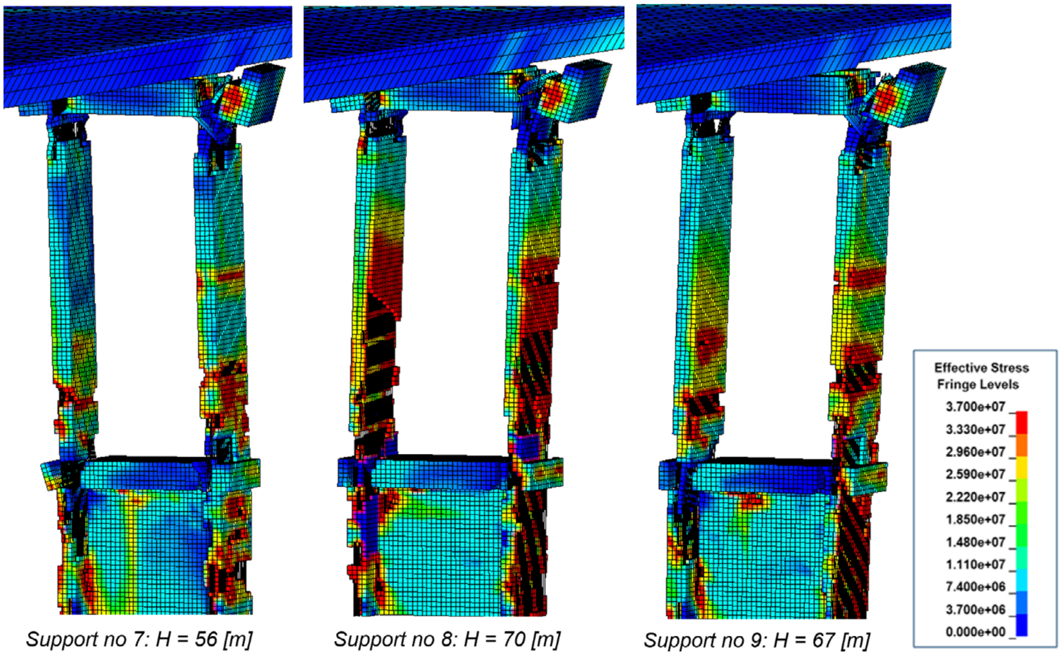

FIGURE 20 Degradation of the three highest supports just before their destruction

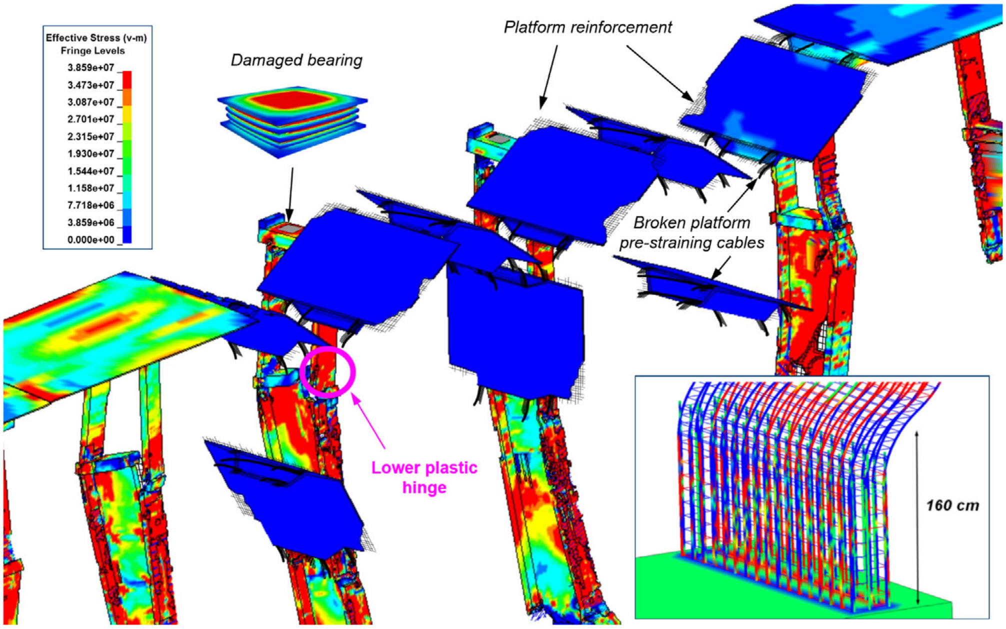

FIGURE 21 Destruction of the V17 viaduct in the 72nd second of the Kocaeli level D3 earthquake

the height of 160 cm, that is, where the reinforcement led from the rigid part of the support ends once the reinforcement rods reach a stain of 442 MPa.

This destruction refers to the destruction of the Hanshin route viaduct supports during the Kobe earthquake in Japan in 1995. After the disaster, an investigation committee led by prof. Hirokazu Lemura from the Kyoto University examined the damaged supports. They found that each support was reinforced by 2 layers of a steel bar. The outer reinforcement layer ran through the entire height of the support from the foundation to the top of the platform. The inner layer of reinforcement consisted of rods coming out of the base of the foundation at the height of 150 cm, to which rods from the outer layer were attached (Figure 22).

FIGURE 22 Destruction of viaduct supports of the Hanshin route (Kobe, 1995)

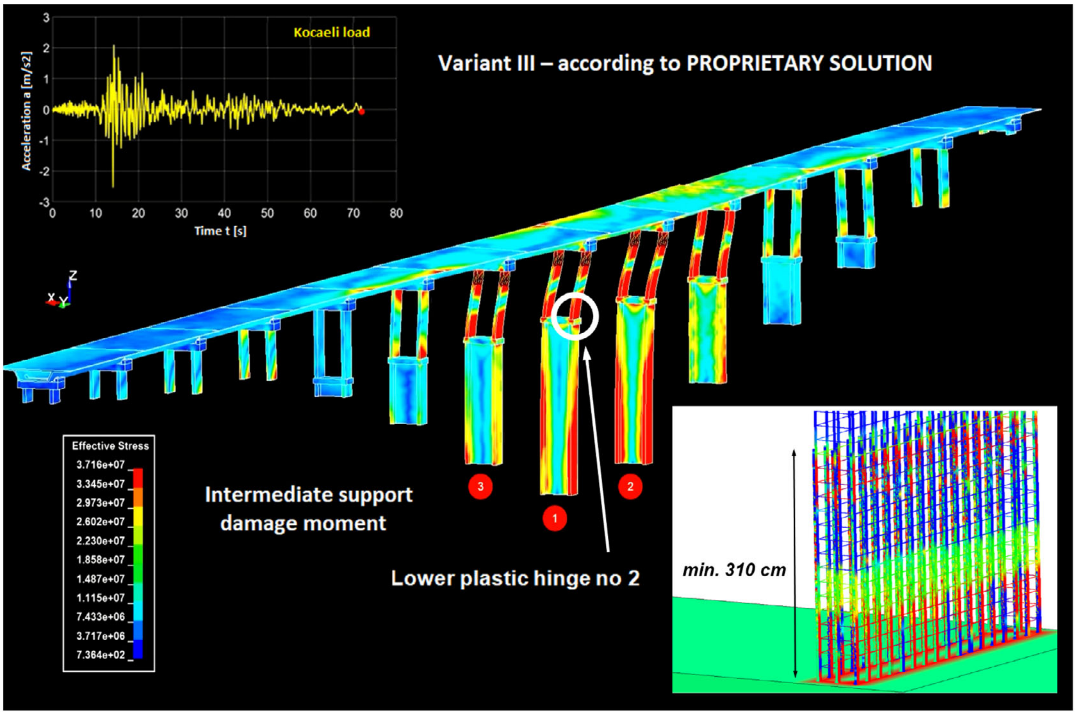

FIGURE 23 Destruction of the V17 viaduct in the 72nd second of the Kocaeli level D3 earthquake

Detailed analyses have proven that major damage to the viaduct occurred at the height of 150 cm to which the reinforcing bars coming out of the foundation were extended. Platform vibrations exerted powerful forces acting on the support, which cracked at their weakest point, where the inner reinforcement layer ended. A plastic hinge was formed at the height of 150–160 cm.

The investigation committee concluded that if the inner reinforcement rods had been longer, the Hanshin route would have withstood the shock.

Another variant subjected to numerical calculation, based on the new DDC2 algorithm to determine the section plasticity, was variant II of the reinforcement formation in the transition zone of the intermediate support. The results obtained during the numerical analysis are presented below (Figure 23).

The stress map shows a zone which indicates that with a reinforcement bond made at a height of at least 310 cm, rods coming out of the rigid part of the support and rods starting in the flaccid part work together perfectly.

With this reinforcement arrangement, the area where maximum stresses concentrate has moved to the very bottom of the joint and the stress value reached 314 MPa, which is much less than the yield point.

Based on the results obtained, we found that only the upper part of the three highest supports will be subjected to controlled destruction and plastification. This will reduce damage to the intermediate supports to a minimum. Potential

FIGURE 24 Photos from the application of the new DDC2 algorithm on the Northern Marmara Highway construction site

repair of the supports could be made under the viaduct platform. The proprietary concept of the new support with variable geometry and stiffness as well as the proprietary reinforcement shape concept based on the new Algorithm 2—DDC2 are the only ones that meet the design requirement for level D3 of the Turkish standard.

Photos from the application of the results obtained based on the new DDC2 algorithm on the construction site of the Istanbul Northern Marmara Highway ring road are presented below (Figure 24).

9 | CONCLUSION

The possibility to use highly efficient calculation algorithms, softwares for structural analysis and supercomputers introduces a new quality in the design, maintenance and repairing processes of engineering structures. In the majority of the building dynamic problems where the inertia forces are marginal it is sufficient to perform calculations within the static scope. In case of quick-change processes, such as impulsive loads resulting from an impact or seismic actions, a dynamic analysis is necessary. The Ls-Dyna software using explicit method and performing parallelized calculations on high-performance computing enables to receive detailed solutions to complicated engineering problems in a relatively short time.

The tasks presented in the article are application examples performed for the purpose of the own scientific paper oriented towards either the cognitive aspects of the material degradation process or the bridge structural elements leading to failure. Nevertheless, they resulted from the real engineering problems, hence they could constitute a material supporting the decision making process on the structure condition, repairing solutions, or design recommendations.

Based on the results obtained we have proven that the DDC method of determining the geometric parameters of plastic joints is far from perfect. It does not reflect the emergence of plastic hinges. This is because it does not take into account the way the reinforcement is joined in the transition zone between the concreted elements on the construction site. This results in a dynamic analysis over-generalization of the structure and consequently leads to incorrect results.

Designing concrete and reinforced concrete elements is based on standard regulations, which are primarily based on the results of experimental research or on in-situ measurements, see Miśkiewicz et al.[52] The formulas proposed in the standards usually result from linear analysis with numerous added safety factors. Such a description of the behavior of concrete and reinforced concrete elements is oversimplified, especially if these elements get thoroughly analyzed. Therefore, it is necessary to account for nonlinear behavior during the loading process, as well as material heterogeneity in their description.

Therefore, we proposed a new DDC2 algorithm for determining the main parameters of plastic hinges depending on the degree of concrete degradation based on the finite element method. The development of a new algorithm allowed for implementation into the actual structure of viaducts as part of the Northern Marmara Highway Istanbul ring road. The newly adopted concept of shaping intermediate support with variable geometry and stiffness based on a proprietary program made it possible to correct the redistribution of internal viaduct forces (in relation to the solution with constant stiffness supports), enabling rationalization of the bridge structure, and consequently reduce construction costs.

It has been shown that the support deflections under load from the D1 and D2 levels are too small to make the support plasticize. However, it is how the reinforcements are made in the transition zone which are decisive for meeting the design requirements for a level D3 Kocaeli load.

Implementation of the new DDC2 algorithm enabled parametric tests for different reinforcement bonding heights in the transition zone. We have also proven that the extension of the assembly rods from the concreted element to a height of 150 cm (which is the commonly accepted height of the assembly rods on the construction site) is an incorrect solution. This conclusion can be supported by the disaster of the Hanshin route viaducts during the 1995 Kobe earthquake (cited in Chapter 7), as well as by analogous results obtained during the analysis of the V17 viaduct with variant I rebar design based on the new DDC2 algorithm. In the above-mentioned examples, the plastic hinge was formed just above the place where assembly rods ended at a height of 160 cm, which led to the complete destruction of the viaduct.

Our proprietary solution for shaping the reinforcement in the transition zone based on the new DDC2 algorithm is the only one that fully meets the design requirements of the Northern Marmara Highway ring road project. It improves the mechanism of plastic hinge formation in the lower part of the flaccid support. The transition zone for bonding the assembly reinforcement at a height of at least 310 cm (assuming $L_{p2}^{\text{zone}} = \max(0.3L_i; 1.5\text{ m})$, where $L_i = 10.5\text{ m}$)) results in controlled destruction and plastification occurring only in the upper part of the flaccid support. This reduces the degradation of the intermediate supports to a minimum, and also makes it possible to repair the supports if necessary. Created based on the finite element method, the detailed and complete calculation model of the bridge structure with detailed consideration of the reinforcement, elastomer bearings, and internal and external prestressing of the platform is more reliable than the models used in practical general engineering design.

The new DDC2 algorithm used in numerical calculations in other facilities may help to prevent failures and damage to viaduct support structures, thus ensuring safety for all users using these facilities.

Based on the results obtained, we have proven that the proposed new DDC2 algorithm and the new concept of shaping intermediate supports with variable geometry and stiffness enriches the bridge structure analysis exposed to earthquakes based on the finite element method.

CONFLICT OF INTEREST

The authors declare that they have no known competing financial interests or personal relationships that could have appeared to influence the work reported in this article.

DATA AVAILABILITY STATEMENT

Research data are not shared.

ORCID

Karol Grębowski https://orcid.org/0000-0003-2342-2970
Krzysztof Wilde https://orcid.org/0000-0001-6878-3126
Mikołaj Miśkiewicz https://orcid.org/0000-0002-6936-6823

REFERENCES

1. Kostovos M, Newman J. Generalized stress–strain relations for concrete. *J Eng Mech ASCE*. 1978;104(4):845-856.
2. Kupfer H, Hilsdorf HK, Rusch H. Behavior of concrete under biaxial stresses. *Am Concr Inst-J*. 1969;66(8):656-666.
3. Hordijk DA. *Local Approach to Fatigue of Concrete*. Dissertation. Delft University of Technology; 1991.
4. Perdikaris PC, Romeo A. Size effect on fracture energy of concrete and stability issues in three-point bending fracture toughness testing. *ACI Mater J*. 1995;92(5):483-496.

5. Mazars J. A description of micro- and macroscale damage of concrete structures. *Eng Fract Mech*. 1986;25:729-737. doi:10.1016/0013-7944(86)90036-6
6. Krajcinovic D, Fonseka GU. The continuous damage theory of brittle materials. Part 1: general theory. *J Appl Mech Trans ASME*. 1981;48:809-815. doi:10.1115/1.3157739
7. Dragon A, Mróz Z. A continuum model for plastic-brittle behaviour of rock and concrete. *Int J Eng Sci*. 1979;17:121-137. doi:10.1016/0020-7225(79)90058-2
8. Carol I, Rizzi E, Willam K. On the formulation of anisotropic elastic degradation. II. Generalized pseudo-Rankine model for tensile damage. *Int J Solids Struct*. 2001;38:519-546. doi:10.1016/S0020-7683(00)00031-7
9. Carol I, Rizzi E, Willam K. On the formulation of anisotropic elastic degradation. I. Theory based on a pseudo-logarithmic damage tensor rate. *Int J Solids Struct*. 2001;38:491-518. doi:10.1016/S0020-7683(00)00030-5
10. Simo JC, Ju JW. Strain- and stress-based continuum damage models—I. Formulation. *Int J Solids Struct*. 1987;23:821-840. doi:10.1016/0020-7683(87)90083-7
11. Carol I, Rizzi E, Willam K. A unified theory of elastic degradation and damage based on a loading surface. *Int J Solids Struct*. 1994;31:2835-2865. doi:10.1016/0020-7683(94)90072-8
12. Ortiz M. A constitutive theory for the inelastic behavior of concrete. *Mech Mater*. 1985;4:67-93. doi:10.1016/0167-6636(85)90007-9
13. Pamin J, de Borst R. Stiffness degradation in gradient-dependent coupled damage-plasticity. *Arch Mech*. 1999;51(3–4):419-446.
14. Lee J, Fenves GL. Plastic-damage model for cyclic loading of concrete structures. *J Eng Mech*. 1998;124:892-900. doi:10.1061/(ASCE)0733-9399
15. Luccioni B, Oller S, Danesi R. Coupled plastic-damaged model. *Comput Methods Appl Mech Eng*. 1996;129:81-89. doi:10.1016/0045-7825(95)00887-X
16. Hansen E, William K, Carol I. A two-surface anisotropic damage/plasticity model for plain concrete. Proceedings of Framcos-4 Conference Fracture Mechanics of Concrete Materials; 2001:549-556.
17. Hansen E. *A Two-Surface Anisotropic Damage/Plasticity Model for Plain Concrete*. Dissertation. University of Colorado at Boulder ProQuest Dissertations Publishing; 2000.
18. Meschke G, Lackner R, Mang HA. An anisotropic elastoplastic-damage model for plain concrete. *Int J Numer Methods Eng*. 1998;42(4):702-727.
19. Bazant ZP, Kim SS. Plastic-fracturing theory for concrete. *ASCE J Eng Mech Div*. 1979;105(3):407-428.
20. Klisiński M, Mróz Z. Description of inelastic deformation and degradation of concrete. *Int J Solids Struct*. 1988;24:391-416. doi:10.1016/0020-7683(88)90070-4
21. Lubliner J, Oliver J, Oller S, Oñate E. A plastic-damage model for concrete. *Int J Solids Struct*. 1989;25:299-326. doi:10.1016/0020-7683(89)90050-4
22. Chróścielewski J, Miśkiewicz M, Pyrzowski Ł, Sobczyk B. Damage analysis of tensioning cable anchorage zone of a bridge superstructure, using CDP Abaqus material model. *Arch Civil Eng*. 2017;63:3-18. doi:10.1515/ace-2017-0025
23. Grassl P, Jirásek M. Damage-plastic model for concrete failure. *Int J Solids Struct*. 2006;43:7166-7196. doi:10.1016/j.ijsolstr.2006.06.032
24. Grębowski K, Hirsz M, Wilde K, Nadolny A. Parametric analysis of Istanbul's ring road viaduct for three levels of seismic load. Proceedings of the 3rd Polish Congress of Mechanics, PCM 2015 and 21st International Conference on Computer Methods in Mechanics Advances in Mechanics: Theoretical, Computational and Interdisciplinary Issues, CMM 2015; 2016. doi:10.1201/b20057‐46
25. Grębowski K, Werdon M. Cable-stayed cantilever structures as an expat of unique application in the construction of a building located in seismic area—an author's project of multifunctional building in Lisbon, Portugal. *Int J Appl Mech Eng*. 2015;20:805-816. doi:10.1515/ijame-2015-0052
26. Zhao XM, Wu YF, Leung AYT. Analyses of plastic hinge regions in reinforced concrete beams under monotonic loading. *Eng Struct*. 2012;34:466-482. doi:10.1016/j.engstruct.2011.10.016
27. Lasowicz N, Kwiecień A, Jankowski R. Experimental study on the effectiveness of polyurethane flexible adhesive in reduction of structural vibrations. *Polymers*. 2020;12:2364. doi:10.3390/polym12102364
28. Stręk AM, Lasowicz N, Kwiecień A, Zając B, Jankowski R. Highly dissipative materials for damage protection against earthquake-induced structural pounding. *Materials*. 2021;14:3231. doi:10.3390/ma14123231
29. Oller S, Oñate E, Oliver J, Lubliner J. Finite element nonlinear analysis of concrete structures using a plastic-damage model. *Eng Fract Mech*. 1990;35:219-231. doi:10.1016/0013-7944(90)90200-Z
30. Ortiz M, Simo JC. An analysis of a new class of integration algorithms for elastoplastic constitutive relations. *Int J Numer Methods Eng*. 1986;23:353-366. doi:10.1002/nme.1620230303
31. Simo JC, Ortiz M. A unified approach to finite deformation elastoplastic analysis based on the use of hyperelastic constitutive equations. *Comput Methods Appl Mech Eng*. 1985;49:221-245. doi:10.1016/0045-7825(85)90061-1
32. Brinkgreve R. *Geomaterial Models and Numerical Analysis of Softening*. Technische Universiteit Delft; 1994.
33. Vermeer PA, Brinkgreve RBJ. A new effective non-local strain measure for softening plasticity. International Workshop on Localisation and Bifurcation Theory for Soils and Rocks; 1994:89-100.
34. Benvenuti E, Tralli A. Iterative LCP solvers for non-local loading-unloading conditions. *Int J Numer Methods Eng*. 2003;58:2343-2370. doi:10.1002/nme.856
35. Strömberg L, Ristinmaa M. FE-formulation of a nonlocal plasticity theory. *Comput Methods Appl Mech Eng*. 1996;136:127-144. doi:10.1016/0045-7825(96)00997-8

36. Zhang Y, Lorentz E, Besson J. Ductile damage modelling with locking-free regularised GTN model. *Int J Numer Methods Eng*. 2018;113:1871-1903. doi:10.1002/nme.5722
37. Piątek-Sierek E. Kalibracja parametrów określających właściwości betonu opisanego modelem plastyczno-degradacyjnym zaimplementowanym w programie ABAQUS; 2013.
38. Davies J. Observation of the fracture path development in mortar beam specimens. *Adv Cem Bas Mat*. 1996;3:31-36. doi:10.1016/S1065-7355(96)90067-X
39. Miśkiewicz M, Bruski D, Chróścielewski J, Wilde K. Safety assessment of a concrete viaduct damaged by vehicle impact and an evaluation of the repair. *Eng Failure Anal*. 2019;106:104147. doi:10.1016/j.engfailanal.2019.104147
40. Ambrosio PD, De Tommasi D, Marzano S. Nonlinear elastic deformations and stability of laminated rubber bearings. *J Eng Mech*. 1995;121:1041-1048. doi:10.1061/(ASCE)0733-9399
41. Iizuka M. A macroscopic model for predicting large-deformation behaviors of laminated rubber bearings. *Eng Struct*. 2000;22:323-334.
42. Abe M, Yoshida J, Fujino Y. Multiaxial behaviors of laminated rubber bearings and their modeling. II: modeling. *J Struct Eng*. 2004;130:1133-1144. doi:10.1061/(ASCE)0733-9445
43. Yoshida J, Abe M, Fujino Y. Constitutive model of high-damping rubber materials. *J Eng Mech*. 2004;130:129-141. doi:10.1061/(ASCE)0733-9399
44. Salomón O, Oller S, Barbat A. Finite element analysis of base isolated buildings subjected to earthquake loads. *Int J Numer Methods Eng*. 1999;46:1741-1761. doi:10.1002/(SICI)1097-0207(19991210)46:10<1741::AID-NME722>3.0.CO;2-H
45. Yoshida J, Abe M, Fujino Y, Watanabe H. Three-dimensional finite-element analysis of high damping rubber bearings. *J Eng Mech*. 2004;130:607-620. doi:10.1061/(ASCE)0733-9399
46. Ogden R. Non-linear elastic deformations. *Eng Anal Bound Elem*. 1984;1:119. doi:10.1016/0955-7997(84)90049-3
47. Hallquist JO. *LS-DYNA: Keyword Users Manual, Version 2018*. Livermore Software Technology Corporation; 2018.
48. Hallquist JO. *LS-DYNA Theoretical Manual*. Livermore Software Technology Corporation; 2018.
49. Caltrans—Seismic Design Criteria; 2004.
50. Kazantzi AK, Vamvatsikos D, Lignos DG. Seismic performance of a steel moment-resisting frame subject to strength and ductility uncertainty. *Eng Struct*. 2014;78:69-77. doi:10.1016/j.engstruct.2014.06.044
51. DLH. The Earthquake Technical Regulation Regarding to the Construction of Port and Harbor Structures, Railways and Airports; 2008.
52. Miśkiewicz M, Mitrosz O, Brzozowski T. Preliminary field tests and long-term monitoring as a method of design risk mitigation: a case study of Gdańsk deepwater container terminal. *Polish Maritime Res*. 2017;24:106-114. doi:10.1515/pomr-2017-0095

How to cite this article: Grębowski K, Wilde K, Miśkiewicz M. Finite element modeling of plastic hinges based on ductility demand-capacity method using nonlinear material for dynamic analysis. *Int J Numer Methods Eng*. 2022;1-40. doi: 10.1002/nme.7170

APPENDIX. ELASTIC–PLASTIC MODEL'S PARAMETERS WITH STIFFNESS DEGRADATION

Young's modulus (Pa)	Poisson's ratio (−)	Dilatation angle (°)	Eccentricity (−)	Biaxial/uniaxial compression plastic strain ratio, f_{b0}/f_{c0} (−)	Parameter, K_c	Viscosity (−)
30,948,281,317	0.167	16	0.07	1.16	0.667	0.001

Stress (Pa)	Inelastic strain (−)	Compressive degradation, d_c (−)	Inelastic strain (−)	Stress (Pa)	Crushing strain (−)	Tensile degradation, d_c (−)	Crushing strain (−)
22,475,967	0	0	0	2,551,987	0	0	0
28,700,146	0.000073	0.04	0.000073	1,465,731	0.000118	0.32	0.000118
33,516,981	0.000167	0.07	0.000167	841,841	0.000303	0.55	0.000303
36,905,533	0.000317	0.11	0.000317	483,511	0.000644	0.7	0.000644
…	…	…	…	277,704	0.00131	0.81	0.00131
845,509	0.009973	0.99	0.0009973	91,608	0.002634	0.99	0.002634